

# THERMOELECTRIC STUDIES OF $p$ -TYPE $\text{Mg}_3\text{Sb}_2$ BASED MATERIALS

McMaster University

Department of Chemistry and Chemical Biology

Thesis Author: Ian Pao

Supervisor: Yuriy Mozharivskyj

## ABSTRACT

This M.Sc thesis investigates *p*-type  $\alpha$ -Mg<sub>3</sub>Sb<sub>2</sub> based thermoelectric materials. High-performance Mg<sub>3</sub>Sb<sub>2</sub> based materials are typically doped with expensive and scarce elements such as Te<sup>3,4,5</sup>, Nd<sup>6,7</sup>, Gd<sup>8,9</sup>, Ho<sup>8</sup>, Yb<sup>10,11,12,15</sup>, Eu<sup>13,14</sup> ... etc. In this study, cheap and abundant dopants such as Zn, Na, Cd, Bi, Pb etc. were attempted. Zn & Na co-doping as well as Zn & Ag co-doping has shown promising thermoelectric properties. Cd doped Mg<sub>3</sub>Sb<sub>2</sub> materials have shown thermal instability at high temperatures which led to thermal decomposition. The co-doping of Zn & Bi, Pb and K has failed.

Pure phase Mg<sub>3</sub>Sb<sub>2</sub> is inherently a *p*-type material. However, the *n*-type materials achieve much higher thermoelectric figure of merit *zT* value than their *p*-type counterparts. The best performing *n*-type Mg<sub>3.15</sub>Mn<sub>0.05</sub>Sb<sub>1.5</sub>Bi<sub>0.49</sub>Te<sub>0.01</sub> possesses an average *ZT* ~1.25 (from 300 K to 723 K) and a peak *ZT* 1.85 at 723 K (Chen et al., 2018)<sup>1</sup>, whereas *p*-type YbCd<sub>1.85</sub>Mn<sub>0.15</sub>Sb<sub>2</sub> has the highest figure of merit *ZT* of 1.14 at 650 K (Guo et al., 2011)<sup>2</sup>.

## ACKNOWLEDGEMENTS

My supervisor Professor Yuriy Mozharviskyj and Dr. Timothy Lo have offered me a tremendous amount of guidance and help throughout my M.Sc. journey, without them I would not have a dedicated research project, nor would I be able to do research at all. I would like to thank Professor Emeritus Gary J. Schrobilgen for his guidance during my undergraduate studies and encouraged me to pursue Chemistry. I appreciate all the input from my committee members, my supervisor and Professor Peter Kruse, on the progress of my research. I am thankful to have worked with Dr. Yu-Chih Tseng from CanmetMATERIALS Natural Resources Canada, allowing me to gain experience in a federal government research lab setting and use the facilities' instruments for my, and my colleague's research; Dr. Shaochang Song for offering aid to our lab and providing us tools for materials production. I am grateful to my lab groupmates and colleagues for their continuous support.

Last but not least, I would like to thank my parents for their continuous support on my academic journey and, my friends who constantly bug me to play online video games that I hate to maintain my sanity.

# TABLE OF CONTENTS

## *Chapter 1. Introduction*

|            |                                  |           |
|------------|----------------------------------|-----------|
| <b>1.1</b> | <b>Thermoelectric effect</b>     | <b>12</b> |
| 1.1.1      | Seebeck effect                   | 12        |
| 1.1.2      | Peltier effect                   | 13        |
| <b>1.2</b> | <b>Thermoelectric properties</b> | <b>14</b> |
| 1.2.1      | Electrical properties            | 16        |
| 1.2.2      | Thermal properties               | 19        |
| 1.2.3      | Phonon scattering                | 19        |
| 1.2.4      | Intrinsic and extrinsic doping   | 20        |

## *Chapter 2. Methodology*

|            |   |           |
|------------|---|-----------|
| <b>2.1</b> | <b>Synthesis methods</b>                                      | <b>23</b> |
| 2.1.1      | Ball milling  | 23        |
| 2.1.2      | Spark plasma sintering  | 24        |
| <b>2.2</b> | <b>Sample characterization</b>                                | <b>25</b> |
| 2.2.1      | Powder x-ray diffraction                                      | 25        |
| 2.2.2      | Scanning Electron Microscope / Energy Dispersive Spectroscopy | 26        |
| <b>2.3</b> | <b>Properties measurement</b>                                 | <b>29</b> |
| 2.3.1      | Electrical properties measurement                             | 29        |
| 2.3.2      | Thermal properties measurement                                | 30        |

|  |                                   |           |
|--|-----------------------------------|-----------|
|  | <i>References (Chapter 1 – 2)</i> | <b>32</b> |
|--|-----------------------------------|-----------|

***Chapter 3. Thermoelectric studies of p-type Zn, Na and Ag doped Mg<sub>3</sub>Sb<sub>2</sub> based thermoelectric materials***

|            |                                 |           |
|------------|---------------------------------|-----------|
| <b>3.1</b> | <b>Abstract</b>                 | <b>39</b> |
| <b>3.2</b> | <b>Introduction</b>             | <b>39</b> |
| <b>3.3</b> | <b>Experimental</b>             | <b>40</b> |
| <b>3.4</b> | <b>Results and discussions</b>  | <b>42</b> |
| 3.4.1      | PXRD and SEM/EDS phase analysis | 45        |
| 3.4.2      | Electronic transport properties | 46        |
| 3.4.3      | Thermal transport properties    | 49        |
| <b>3.5</b> | <b>Conclusions</b>              | <b>51</b> |

***Chapter 4. Thermoelectric studies of p-type Cd and Na co-doped Mg<sub>3</sub>Sb<sub>2</sub> based materials***

|            |   |           |
|------------|---|-----------|
| <b>4.1</b> | <b>Abstract</b>   | <b>52</b> |
| <b>4.2</b> | <b>Introduction</b>   | <b>52</b> |
| <b>4.3</b> | <b>Experimental</b>   | <b>52</b> |
| <b>4.4</b> | <b>Results and discussions</b>                                    | <b>53</b> |
| 4.4.1      | PXRD and SEM/EDS phase analysis                                   | 54        |
| 4.4.2      | Electronic transport properties                                   | 57        |
| 4.4.3      | Thermal decomposition of Cd doped Mg <sub>3</sub> Sb <sub>2</sub> | 58        |
| <b>4.5</b> | <b>Conclusions</b>  | <b>59</b> |

***Chapter 5. Failure of Zn/K co-doping in p-type Mg<sub>3</sub>Sb<sub>2</sub> based thermoelectric material***

|            |                                 |           |
|------------|---------------------------------|-----------|
| <b>5.1</b> | <b>Abstract</b>                 | <b>60</b> |
| <b>5.2</b> | <b>Introduction</b>             | <b>60</b> |
| <b>5.3</b> | <b>Experimental</b>             | <b>60</b> |
| <b>5.4</b> | <b>Results and discussions</b>  | <b>61</b> |
| 5.4.1      | PXRD and SEM/EDS phase analysis | 62        |
| 5.4.2      | Electronic transport properties | 62        |
| <b>5.5</b> | <b>Conclusions</b>              | <b>63</b> |

***Chapter 6. Failure of Zn/Bi co-doping in p-type Mg<sub>3</sub>Sb<sub>2</sub> based thermoelectric material***

|            |                                 |           |
|------------|---------------------------------|-----------|
| <b>6.1</b> | <b>Abstract</b>                 | <b>64</b> |
| <b>6.2</b> | <b>Introduction</b>             | <b>64</b> |
| <b>6.3</b> | <b>Experimental</b>             | <b>64</b> |
| <b>6.4</b> | <b>Results and discussions</b>  | <b>65</b> |
| 6.4.1      | PXRD and SEM/EDS phase analysis | 65        |
| <b>6.5</b> | <b>Conclusions</b>              | <b>67</b> |

***Chapter 7. Failure of Pb doping in p-type Mg<sub>3</sub>Sb<sub>2</sub> based thermoelectric material***

|            |                                       |           |
|------------|---------------------------------------|-----------|
| <b>7.1</b> | <b>Abstract</b>                       | <b>68</b> |
| <b>7.2</b> | <b>Introduction</b>                   | <b>68</b> |
| <b>7.3</b> | <b>Experimental</b>                   | <b>68</b> |
| <b>7.4</b> | <b>Results and discussions</b>        | <b>69</b> |
|            | 7.4.1 PXRD and SEM/EDS phase analysis | 69        |
| <b>7.5</b> | <b>Conclusions</b>                    | <b>72</b> |

***Chapter 8. Na/Bi co-doping in p-type Mg<sub>3</sub>Sb<sub>2</sub> based thermoelectric material***

|            |                                       |           |
|------------|---------------------------------------|-----------|
| <b>8.1</b> | <b>Abstract</b>                       | <b>73</b> |
| <b>8.2</b> | <b>Introduction</b>                   | <b>73</b> |
| <b>8.3</b> | <b>Experimental</b>                   | <b>73</b> |
| <b>8.4</b> | <b>Results and discussions</b>        | <b>74</b> |
|            | 8.4.1 PXRD and SEM/EDS phase analysis | 74        |
|            | 8.4.2 Electronic transport properties | 76        |
| <b>8.5</b> | <b>Conclusions</b>                    | <b>77</b> |

***Chapter 9. Thesis conclusion*** **78**

***Chapter 10. Future works*** **79**

***References (Chapter 3 – 8)*** **80**

**Supplementary Information** **85**



## LIST OF SYMBOLS & ABBREVIATIONS

| Symbol             | Description  |
|--------------------|--|
| $\sigma$           | Electrical conductivity  |
| $\sigma_h$         | Holes contribution to electrical conductivity                  |
| $\sigma_e$         | Electrons contribution to electrical conductivity              |
| $\rho$             | Electrical resistivity   |
| S                  | Seebeck coefficient  |
| $S_e$              | Seebeck coefficient of electrons                               |
| $S_h$              | Seebeck coefficient of holes                                   |
| $\pi$              | Peltier coefficient  |
| PF                 | Power factor   |
| $\kappa$           | Thermal conductivity   |
| $\kappa_{tot}$     | Total thermal conductivity                                     |
| $\kappa_L$         | Lattice thermal conductivity                                   |
| $\kappa_e$         | Electronic thermal conductivity                                |
| $\kappa_{eNa0.03}$ | Electronic thermal conductivity of Na = 0.03 doped composition |
| $\kappa_{eAg0.03}$ | Electronic thermal conductivity of Ag = 0.03 doped composition |
| $zT$               | Thermoelectric figure of merit                                 |
| D                  | Thermal diffusivity  |
| V                  | Electrical voltage   |
| $V_{hot}$          | Electrical voltage on hot gradient                             |
| $V_{cold}$         | Electrical voltage on cold gradient                            |
| I                  | Electrical current   |
| T                  | Temperature  |
| $T_{hot}$          | Temperature of hot gradient                                    |
| $T_{cold}$         | Temperature of cold gradient                                   |
| K                  | Kelvin (Unit of temperature)                                   |
| °C                 | Degree Celsius (Unit of temperature)                           |
| L                  | Lorenz number  |

|                 |  |
|-----------------|--|
| $C_p$           | Specific heat capacity                               |
| $N$             | Number of atoms per formula unit                     |
| $R$             | Ideal gas constant (8.314 J/mol·K)                   |
| $M_w$           | Molecular weight                                     |
| $e$             | Elementary charge ( $1.602 \times 10^{-19}$ C)       |
| $\dot{Q}$       | Rate of heat generation                              |
| $\rho$          | Mass density   |
| $m$             | Mass   |
| $m^*$           | Effective mass                                       |
| $m_e^*$         | Effective mass of electrons                          |
| $m_h^*$         | Effective mass of holes                              |
| $e^-$           | Electron   |
| $h^+$           | Hole   |
| $\eta$          | Carrier concentration                                |
| $\eta_{Na0.03}$ | Carrier concentration of Na = 0.03 doped composition |
| $\eta_{Ag0.03}$ | Carrier concentration of Ag = 0.03 doped composition |
| $\eta_e$        | Electron concentration                               |
| $\eta_h$        | Hole concentration                                   |
| $\mu$           | Carrier mobility                                     |
| $\mu_{Na0.03}$  | Carrier mobility of Na = 0.03 doped composition      |
| $\mu_{Ag0.03}$  | Carrier mobility of Ag = 0.03 doped composition      |
| $\mu_e$         | Electron mobility                                    |
| $\mu_h$         | Hole mobility  |
| $\tau$          | Scattering relaxation time                           |
| $\tau_e$        | Scattering relaxation time of electrons              |
| $\tau_h$        | Scattering relaxation time of holes                  |
| $\tau_{e-ph}$   | Electron-phonon scattering relaxation time           |
| $\tau_{im}$     | Impurity scattering relaxation time                  |
| $E_g$           | Band gap energy                                      |
| $k_B$           | Boltzmann's constant ( $8.617 \times 10^{-5}$ eV·K)  |
| $\rho_T$        | Temperature dependence resistivity                   |

|                      |  |
|----------------------|--|
| $\rho_{\text{im}}$   | Resistivity due to impurities                  |
| $\rho_{\text{de}}$   | Resistivity due to lattice defects             |
| $\rho_{\text{e-ph}}$ | Resistivity due to electron-phonon scattering  |
| DOS                  | Density of states                              |
| $E_{\text{f}}$       | Fermi energy                                   |
| $\eta(E_{\text{f}})$ | Concentration of electrons at the Fermi energy |
| $v_{\text{f}}$       | Fermi velocity of electrons                    |
| RPM                  | Rotation per minute                            |
| TEG                  | Thermoelectric generator                       |
| BM                   | Ball mill                                      |
| BM                   | Ball milled composition                        |
| SPS                  | Spark Plasma Sintering                         |
| SPS                  | Sintered composition                           |
| DC                   | Direct current                                 |
| AC                   | Alternating current                            |
| PXRD                 | Powder x-ray diffraction                       |
| SEM                  | Scanning electron microscopy                   |
| TEM                  | Transmission electron microscopy               |
| EDS                  | Energy dispersive spectroscopy                 |
| EPMA                 | Electron probe microanalyzer                   |
| CFT                  | Crystal field theory                           |
| CFSE                 | Crystal field stabilization energy             |
| DMSO                 | Dimethyl sulfoxide                             |

# Chapter 1. Introduction

## 1.1 Thermoelectric effect

Thermoelectric effect is the direct energy conversion between temperature gradient and electric voltage <sup>16</sup>. It is a reversible phenomenon where a temperature difference within a material generates electromotive force; an induced electrical current can produce temperature gradient within the material <sup>17</sup>.

### 1.1.1 Seebeck effect

When a material is placed into a temperature gradient, a voltage is generated across the material. This can be described with the equation:

$$S = -\frac{\Delta V}{\Delta T} = \frac{V_{hot} - V_{cold}}{T_{hot} - T_{cold}} \quad (1 - 1)$$

where  $\Delta V$  is the difference electric potential,  $\Delta T$  is the temperature gradient and  $S$  is the Seebeck coefficient. The sign of the Seebeck coefficient is dependent on the material, which can be either positive ( $p$ -type) or negative ( $n$ -type), except for superconductors where the Seebeck coefficient is always zero <sup>18</sup>. The Seebeck coefficient of a material varies with temperature.

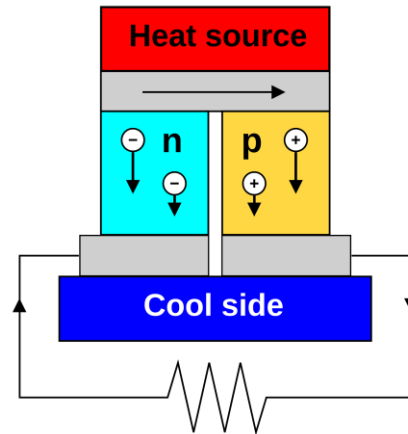


Figure 1.1. Seebeck circuit, indicating current flow direction, heat source (red), cool side (blue),  $n$ -type material (n), flow of  $n$ -type charge carrier (electrons,  $-$ ),  $p$ -type material (p) and flow of  $p$ -type charge carrier (holes,  $+$ ).

For practical applications,  $p$ - and  $n$ -type thermoelectric materials are joined in parallel to optimize the voltage output (Figure 1.1). Seebeck effect is used in thermocouples to measure temperature, and in thermoelectric generators (TEGs) to directly convert heat energy into electricity.

### 1.1.2 Peltier effect

Peltier effect is the reverse of Seebeck effect. When an electric current is applied to a loop of two different materials, a temperature difference is generated: one junction absorbs heat and the other generates heat. The Peltier coefficient ( $\pi$ ) is expressed as:

$$\pi = \frac{\dot{Q}}{I} \quad (1 - 2)$$

$\dot{Q}$  is the rate of heat generation, and  $I$  is the electric current.

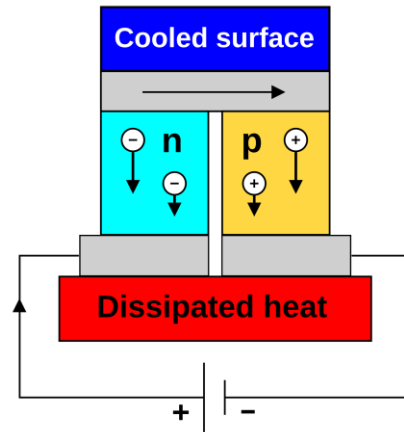


Figure 1.2. Peltier circuit, indicating current flow direction with an applied electrical current. Hot side (red), cool side (blue), *n*-type material (n), flow of *n*-type charge carrier (−), *p*-type material (p) and flow of *p*-type charge carrier (+).

Since the Peltier effect creates temperature difference, it is utilized in thermoelectric cooling devices (refrigeration) and, less commonly in heating.

## 1.2 Thermoelectric properties

The “usefulness” or efficiency of a material is determined by its thermoelectric figure of merit ( $zT$ ) value, which depends on the material’s electrical conductivity ( $\sigma$ ) or electrical resistivity ( $\rho$ ), thermal conductivity ( $\kappa$ ), and Seebeck coefficient ( $S$ ):

$$zT = \frac{S^2 \sigma T}{\kappa} \quad \text{or} \quad zT = \frac{S^2 T}{\rho \kappa} \quad (1 - 3)$$

A material with a high  $zT$  value should have high  $S$  and  $\sigma$  but low  $\kappa$ . However, achieving a desirable  $zT$  value is often challenging as all the parameters are correlated to each other.

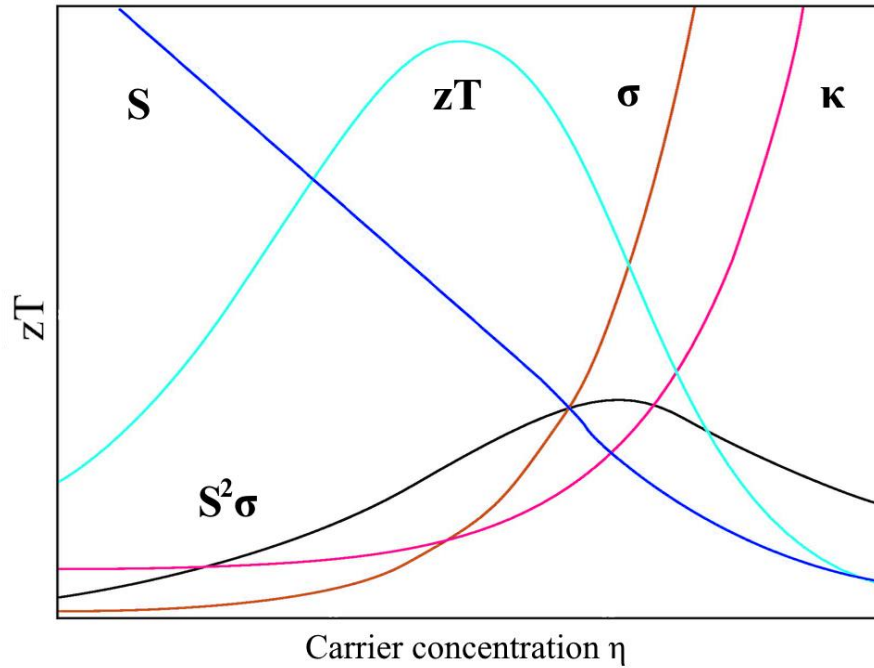


Figure 1.3. Thermoelectric parameters as a function of the carrier concentration. Seebeck coefficient ( $S$ ), electrical conductivity ( $\sigma$ ), thermal conductivity ( $\kappa$ ), power factor ( $S^2\sigma$ ) and figure of merit ( $zT$ ).

Optimization of thermoelectric parameters is a big challenge. As one parameter is enhanced, the other parameters usually become less desirable. For example, an increase in electrical conductivity ( $\sigma$ ) by introducing more carriers ( $\eta$ ) via doping will increase the electrical thermal conductivity ( $\kappa_e$ ), resulting in an increase of the total thermal conductivity ( $\kappa_{tot}$ ).

### 1.2.1 Electrical properties

Electrical conductivity ( $\sigma$ ) determines the material's ability to conduct electric current. It is the reciprocal of electrical resistivity ( $\rho$ ):

$$\sigma = \frac{1}{\rho} \quad (1 - 4)$$

Under most circumstances, only one type of charge carrier species at a time is considered.

However, when multiple charge carrier species (electrons  $e^-$  and holes  $h^+$ ) are both present at certain conditions in a semiconductor, the total  $\sigma$  is the sum of the individual charge carrier conductivities:

$$\sigma_{tot} = \sigma_e + \sigma_h \quad (1 - 5)$$

Where  $\sigma_{tot}$  is the total electrical conductivity,  $\sigma_e$  is the electrical conductivity of electrons and  $\sigma_h$  is the electrical conductivity of holes.

In the semi-classical Drude model, electrical conductivity  $\sigma$  is determined by the charge carrier concentration ( $\eta$ ), carrier mobility ( $\mu$ ) and carrier charge ( $e$ )<sup>19, 20</sup>:

$$\sigma = \eta e \mu = \eta_e e \mu_e + \eta_h e \mu_h \quad (1 - 6)$$

It is assumed that the charge carrier velocity is zero when a scattering event happens. After the event, the carrier accelerates uniformly until another scattering event<sup>21</sup>. Average drift mobility:

$$\mu = \frac{e\tau}{m^*} \quad (1 - 7)$$

Where  $\tau$  is the scattering relaxation time of the charge carrier, and  $m^*$  is the carrier effective mass. The charge carrier mobility,  $\mu$ , is inversely proportional to the effective mass,  $m^*$ , as heavier carriers require more electromotive force to move<sup>21</sup>. By substituting  $\mu = \frac{e\tau}{m^*}$  into  $\sigma = \eta e \mu$ , the following equation is obtained:

$$\sigma = \frac{\eta e^2 \tau}{m^*} \quad (1 - 8)$$



For metals, electrical conductivity  $\sigma$  decreases with increasing temperature  $T$ . As atoms gain energy and vibration intensifies, the electrons' collision probability increases, which increases electron scattering. This reduces charge carrier mobility  $\mu$ , resulting in low  $\sigma$ .

For intrinsic semiconductors to effectively conduct electricity, a sufficient amount of thermal energy must be applied to excite charge carriers to overcome the band gap:

$$\sigma = \frac{\eta e^2 \tau}{m^*} e^{\left(\frac{-E_g}{2k_B T}\right)} \quad (1 - 9)$$

Where  $E_g$  is the band gap energy and  $k_B$  is Boltzmann's constant ( $8.617 \times 10^{-5} \text{ eV} \cdot \text{K}$ ).

$\sigma$  increases with  $T$  as electrons from the valence band are excited into the conduction band, generating holes in the valence band. Such activation of charge carriers is known as bipolar effect: two different species of charge carriers,  $e^-$  and  $h^+$ , participate in the conduction of electricity <sup>22</sup>.

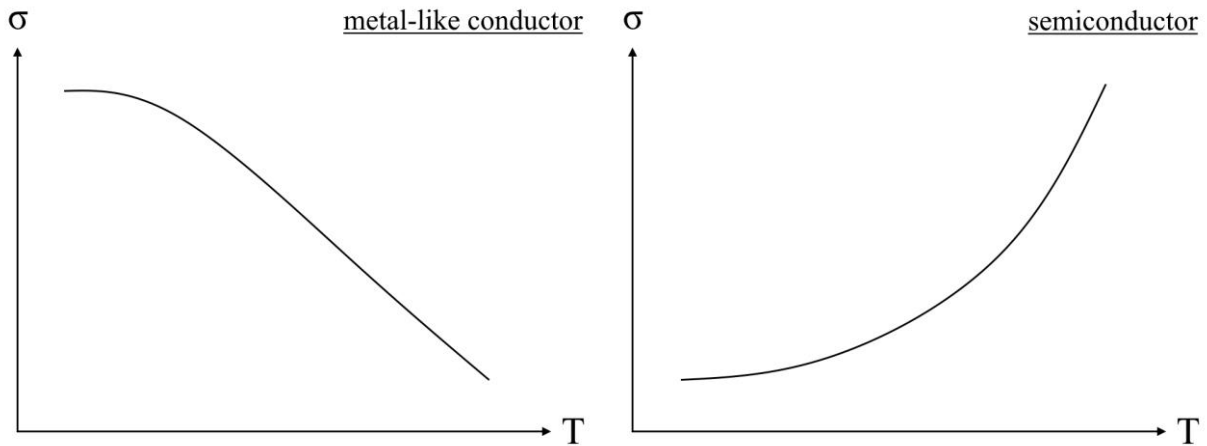


Figure 1.4. Temperature dependence of electrical conductivity ( $\sigma$ ) in metal-like conductors (left) and semiconductors (right).

Ideally, as metals approach 0 K, their electrical conductivity  $\sigma$  should increase to infinity as there are no thermal vibrations that cause carrier scattering in the lattice. However, there is still

“residual” resistivity. Thus, other scattering mechanisms such as defects (grain boundaries, vacancies and dislocations etc.) and impurities in the structure cause scattering. Using Matthiessen’s rule, we can incorporate all the scattering mechanisms into total resistivity ( $\rho_{tot}$ ) of a metal:

$$\rho_{tot} = \rho_T + \rho_{im} + \rho_{def} \quad (1 - 10)$$

Where  $\rho_T$  is the temperature dependence resistivity,  $\rho_{im}$  is resistivity caused by impurities and  $\rho_{def}$  is resistivity caused by lattice defects.

The main distinguishing factor between metals and semiconductors is that metals do not possess any band gap, and they have many delocalized electrons due to high density of states (DOS) at the Fermi level and empty states right above the Fermi level<sup>23</sup>. Due to this, electrons in metals can be treated as free charge carriers traveling through a matrix. As electrons travel, they will interact with individual atoms in the metal, resulting in scattering phenomenon and decreasing  $\sigma$ <sup>24, 25</sup>.

$$\sigma = \frac{e^2 v_f^2 \tau \cdot \eta(E_f)}{3} \quad (1 - 11)$$

$v_f$  is the Fermi velocity of electrons,  $\eta(E_f)$  is the density of electrons at the Fermi energy.

### 1.2.2 Thermal properties

The total thermal conductivity ( $\kappa_{tot}$ ) of a material has a lattice component and an electronic component:

$$\kappa_{tot} = \kappa_e + \kappa_L \quad (1 - 13)$$

Using the Wiedemann-Franz Law <sup>26</sup>, we can expand the electronic component into:

$$\kappa_e = L\sigma T = L(\eta e\mu)T \quad (1 - 14)$$

where L is the Lorenz factor, which is a constant but can deviate depending on the Fermi level of the material. An estimation of Lorenz factor at any temperature can be determined from the experimental measured thermopower |S|: <sup>27</sup>

$$L = \frac{1.5 + \exp\left(\frac{-|S|}{\frac{116\mu V}{K}}\right)}{10^{-8}W\Omega K^{-2}} \quad (1 - 15)$$

The lattice thermal conductivity ( $\kappa_L$ ) can be calculated by:

$$\kappa_L = \kappa_{tot} - L\sigma T \quad (1 - 16)$$

where  $\kappa_{tot}$  is the measured total thermal conductivity of the material,  $\sigma$  is the measured electrical conductivity and, L is the estimated Lorenz factor calculated from measured thermopower |S|.

### 1.2.3 Phonon scattering

Above 0K, atoms are not stationary as they vibrate inside the crystal periodically. A phonon is an elastic arrangement of atoms that consist of collective excitation or oscillation in a periodic frequency. Phonons can be considered as quantized sound waves, where they traverse across a crystal lattice with a periodic wave-like behavior.

Electron-phonon scattering (subscript e-ph) is responsible for the temperature dependence of the electrical resistivity; higher temperatures increase electron-phonon scattering and electrical resistivity increases ( $\rho_{e-ph}$  is the same as  $\rho_T$  as introduced in Chapter 1.2.1).

Phonons carry heat and they are responsible for the lattice thermal conductivity,  $\kappa_L$ , of the solids. Interaction of phonons between themselves, with crystal boundaries, impurities, and defects will dictate the thermal conductivity of materials. However, phonon scattering processes are dependent on temperature and structure, one scattering mechanism may dominate at certain temperatures and certain scattering mechanisms may not be present in some materials. For example, mass difference impurity scattering of phonons tends to dominate at low temperatures as increased lattice vibrations (phonons) at these temperatures are restricted by separations between the impurity atoms.

#### **1.2.4 Intrinsic and extrinsic doping**

Intrinsic vacancies and defects in the material's structure can affect carrier concentration and introduce different types of scattering, consequently affecting thermoelectric properties. Such compositional modification is called intrinsic doping. The  $\text{Mg}_3\text{Sb}_2$ , studied in this thesis, is a *p*-type material when prepared from the stoichiometric ratio. By increasing the Mg amount, one can also prepare an *n*-type  $\text{Mg}_3\text{Sb}_2$ .

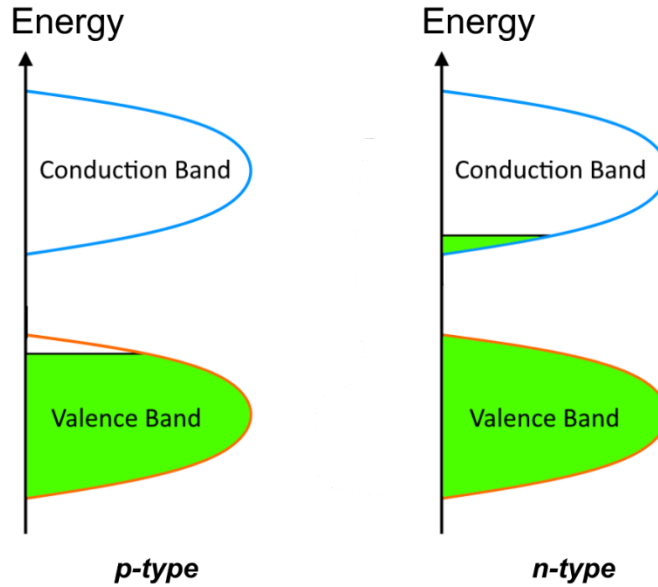


Figure 1.5. Intrinsic doping theoretical effect on valance and conduction band of a semiconductor. *p*-type intrinsic doped semiconductors are electron deficient, indicating formation of holes in the valance band; *n*-type intrinsic doped semiconductors are electron rich, indicating presence of electrons in the conduction band.

Extrinsic doping is achieved by introducing foreign atoms into the structure and can have a variety of effects. When selecting the dopants, their valance electron count and oxidation states are considered. For example, Li<sup>28, 29</sup>, Na<sup>30, 31</sup>, Ag<sup>32, 33</sup>, Cu<sup>34</sup> substituting for Mg; or Ge<sup>35</sup>, Pb<sup>36</sup>, Sn<sup>37</sup> substituting for Sb, will act as *p*-type dopants due to the lower electron concentration. Isoelectronic dopants such as Zn<sup>38, 39, 40</sup>, Cd<sup>41, 42</sup>, Bi will enhance the material's electrical conductivity by narrowing the band gap and lower the lattice thermal conductivity due to increased phonon scattering.

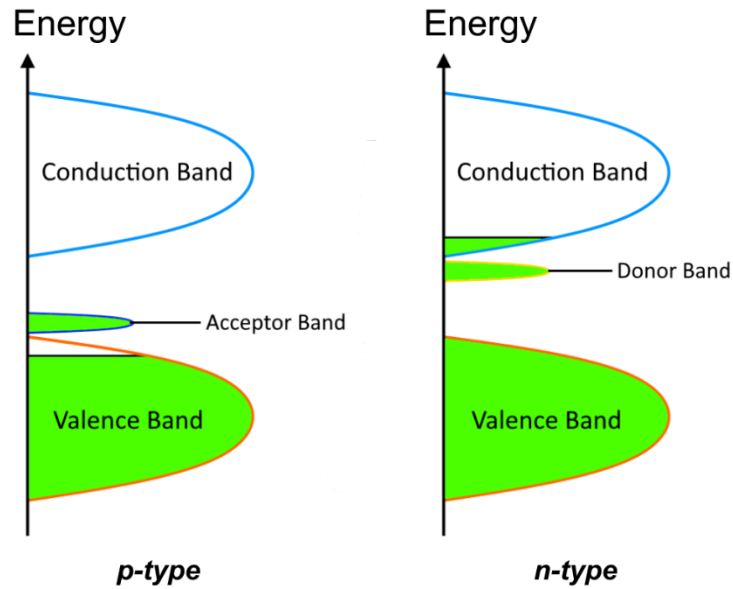


Figure 1.6. Extrinsic doping of elements effect on a semiconductor. Acceptor impurity atoms with lower number of valance electrons accept electrons from intrinsic semiconductor's valance band, providing excess holes to the material. Donor impurity atoms with higher number of valance electrons donate electrons to intrinsic semiconductor's conduction band, providing excess electrons to the material.

## Chapter 2. Methodology

### 2.1 Synthesis methods

#### 2.1.1 Ball milling

Ball milling is a technique used to grind or blend materials. Materials inside a ball mill container are reduced into smaller sized particles by collision and impact from the grinding media, which are usually stainless-steel balls. A planetary ball mill which consists of a grinding jar positioned eccentrically on a “sun wheel”. The rotation direction of the sun wheel is opposite to the rotation direction of the grinding jar; this produces high dynamic energies due to the collision and friction between the steel balls and the grinding jar. These planetary ball mills are also called high energy ball mills.

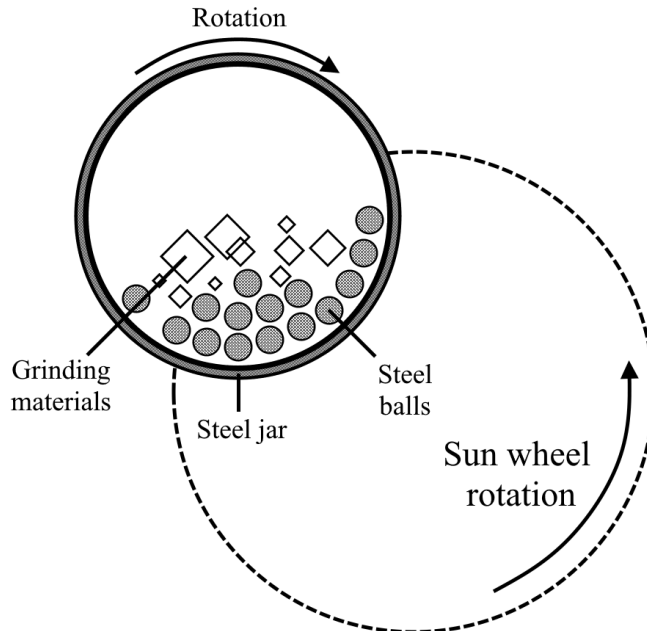


Figure 2.1. Planetary Ball Mill (BM) schematic, indicating the rotation of a steel jar and sun wheel rotation; The “true” rotation per minute (RPM) of grinding content is dependent on the transmission ratio relative to main disk (RPM of steel jar and RPM of sun wheel).

Milling duration, rotational speed, number of milling balls and mass of material will affect the ball milling process. The physical properties of the material for grinding are also considered; one of the limitations for high energy ball mills is the inability to grind soft and chunky materials (sodium, zinc, indium etc.). Hard and brittle materials are ideal for ball milling.

### 2.1.2 Spark plasma sintering

Spark Plasma Sintering (SPS), similar to hot press, is a consolidation method for producing pellet or rod-shaped materials from powdered material. The target powdered material is placed inside a high-density graphite die and between two graphite punches under high pressure. The material and the graphite die are subjected to pulsed DC current joule heating.

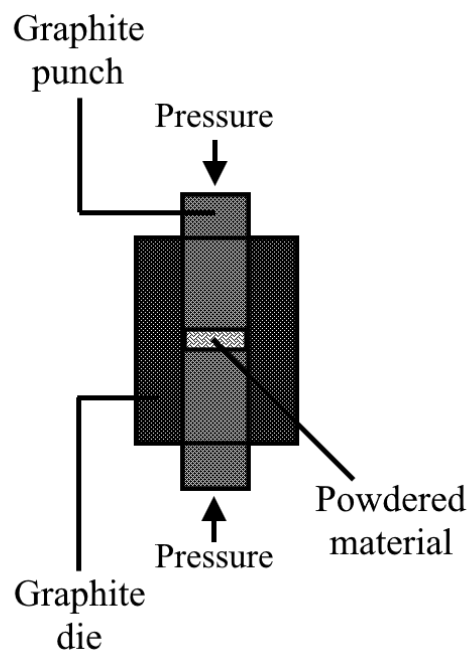


Figure 2.2 Spark Plasma Sintering (SPS) schematic, indicating applied uniaxial pressure on ball milled/powdered material.



One of the advantages of SPS is its internal heat generation, in contrast to traditional hot press; SPS also allows very high heating rate which speeds the densification process.

Sintering temperature, duration and pressure also affect homogeneity, microstructure and the thermoelectric properties of consolidated materials <sup>43</sup>. In general, a long duration sintering allows large grain size and hence increases  $\sigma$  but consequently sacrifices  $\kappa$ . Sintering temperature and applied pressure affects defect formation, dislocations and vacancies, resulting in different types of scattering.

## **2.2 Sample characterization**

### **2.2.1 Powder x-ray diffraction**

Powder X-Ray Diffraction (PXRD) is used for structural analysis and/or phase analysis of crystalline materials. PXRD was performed on a PANalytical X'Pert Pro diffractometer with Co K $\alpha$  radiation (without a monochromator). Powdered samples after ball milling and SPS-consolidated pellets were analyzed. The consolidated samples were grounded to powders before being deposited on a silicon wafer.

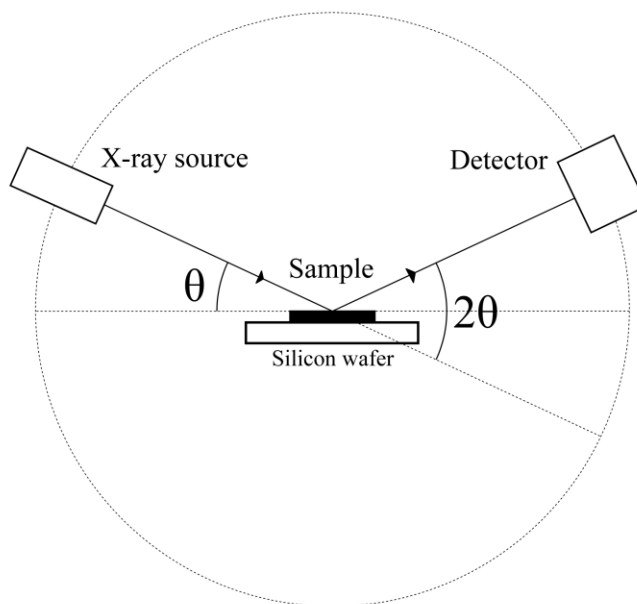


Figure 2.3. Powder X-Ray Diffraction (PXRD) instrument schematic.

The Rietica program was used for the Rietveld refinement of the PXRD data. Phase composition and lattice parameters were obtained from the Rietveld analysis.

### **2.2.2 Scanning Electron Microscope / Energy Dispersive Spectroscopy (SEM/EDS)**

Scanning Electron Microscope (SEM) is used for surface analysis of consolidated, polished pellets. Energy Dispersive Spectroscopy (EDS) is used simultaneously with SEM for elemental composition analysis.

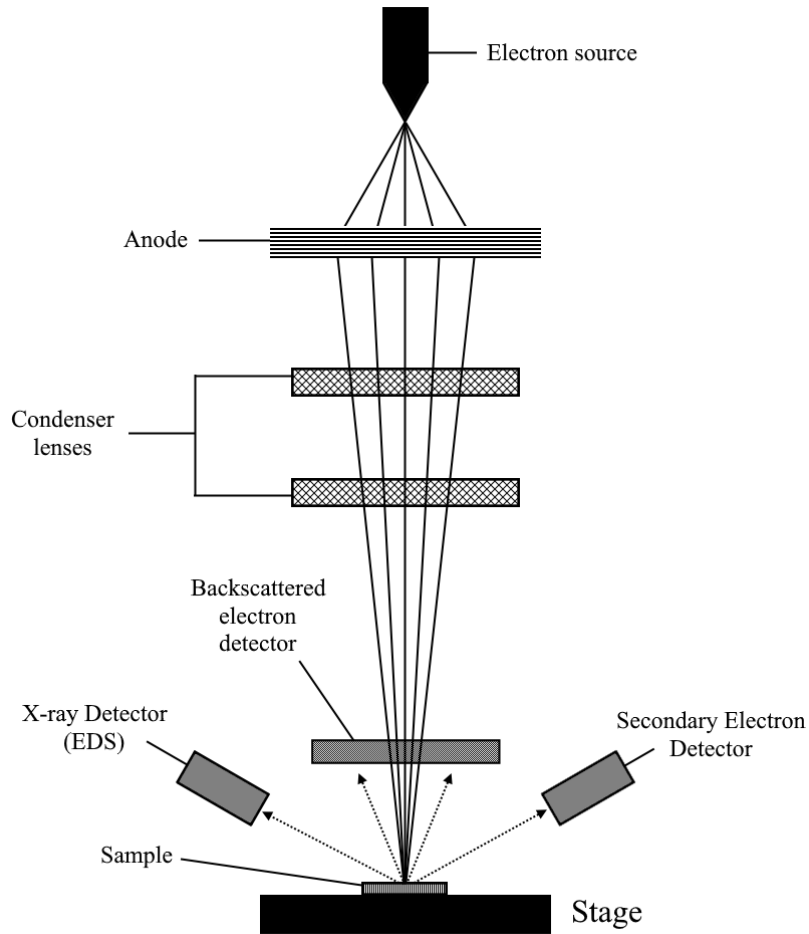


Figure 2.4. Schematics of a SEM/EDS instrument

EDS relies on the X-ray radiation generated by the excited electrons from the atoms in the material. High energy electrons are emitted from the electron beam, and they eject inner electrons from an atom. As an energy electron from a higher energy orbital falls into the vacant orbital, distinctive X-rays are released. This characteristic X-ray is used for the elemental and compositional analysis.

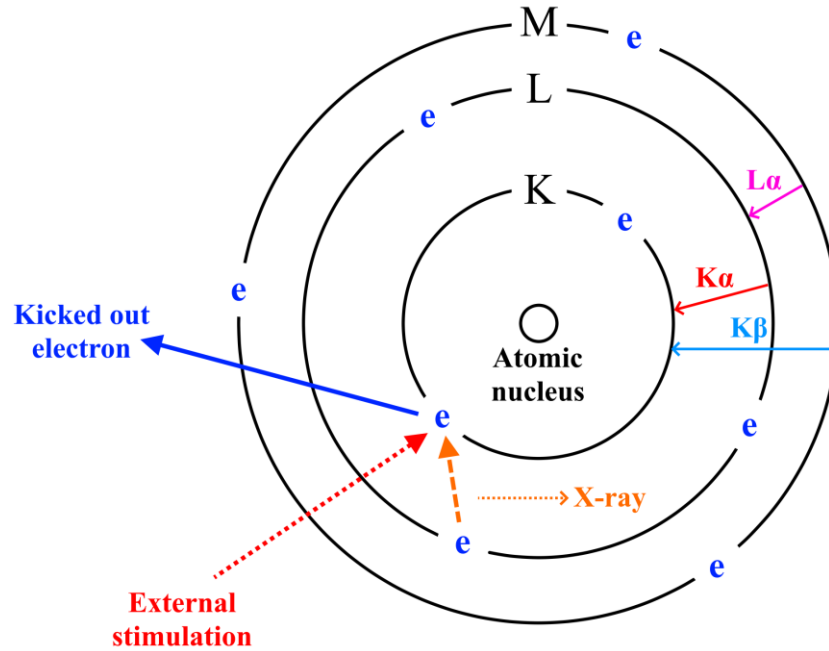


Figure 2.5. Simplified graphical illustration of EDS operation on atomic scale.

K, L and M designate the shell;  $\alpha$  and  $\beta$  refer to the transition. Using the Siegbahn notation, the relaxation of an electron from  $L \rightarrow K$ ,  $M \rightarrow K$ , and  $M \rightarrow L$  is described as  $K_{\alpha}$ ,  $K_{\beta}$ , and  $L_{\alpha}$ .

Overall, EDS is a powerful and versatile technique in determining elemental composition of a material. However, a major drawback of this technique is its inability to detect light elements (Li, Be, B etc., similar to PXRD), since the low energy of their emitted X-rays could not be detected. Moreover, if elements with similar X-ray energies (such as  $Zn-L_{\alpha} = 1.012\text{keV}$  and  $Na-K_{\alpha} = 1.041\text{keV}$ ) are both present in a material, their compositional analysis will be inaccurate as the EDS emission peaks will overlap.

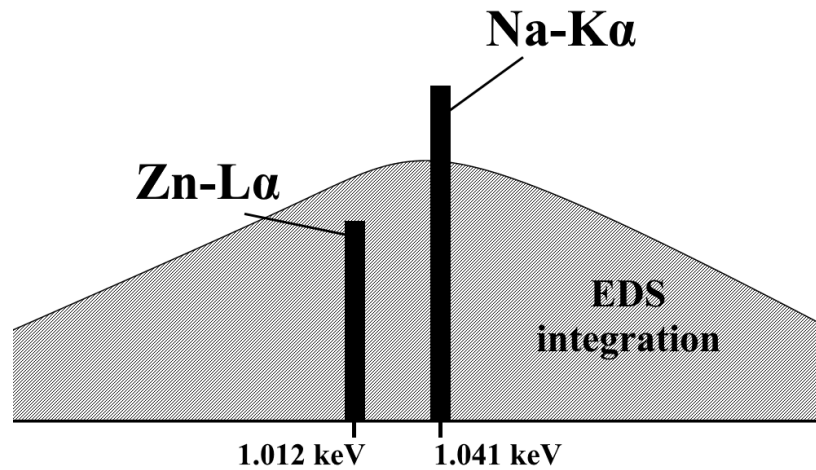


Figure 2.6. Example of SEM/EDS integration limitation on elements with similar dispersive energies.

## 2.3 Properties measurement

### 2.3.1 Electrical properties measurement

Electrical properties such as electrical conductivity, Seebeck coefficients and power factor were measured with the NETZSCH SBA 458 Nemesis instrument, located at CanmetMATERIALS, Natural Resources of Canada, Hamilton, ON. Consolidated 14.7mm diameter sample pellets were placed inside of the instrument with 4-pin electrodes under low pressure environment flushed with argon gas.

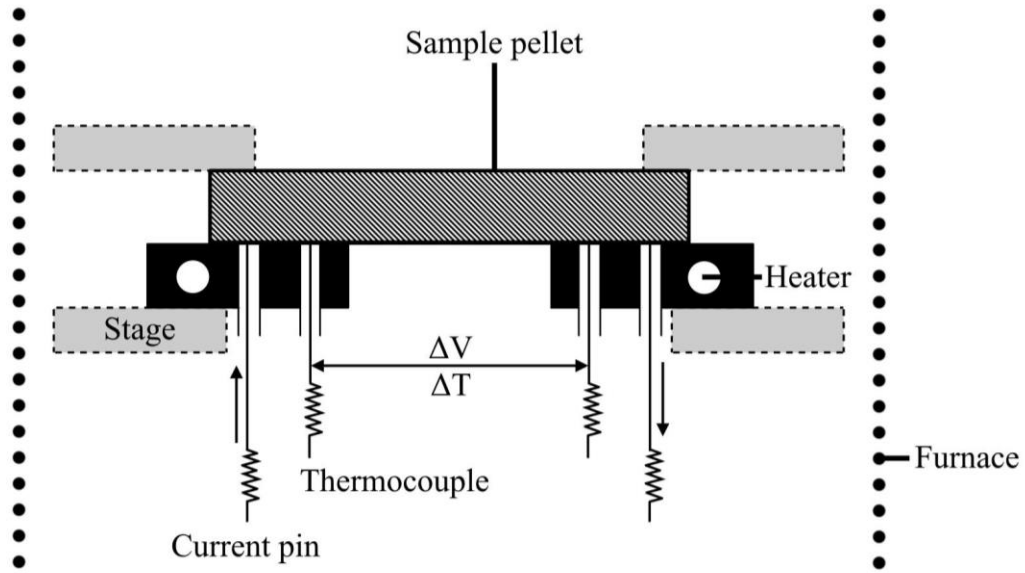


Figure 2.7. Schematics of the NETZSCH SBA 458 Nemesis instrument

An approximate 5 – 15 °C temperature gradient on the circular pellet was used to measure the Seebeck coefficients at various temperatures. With the exception of Pb and Bi containing compositions, electrical properties were measured for all other pellets from 300 K to 773K.

### 2.3.2 Thermal properties measurement

Thermal conductivity is usually derived from experimentally measured thermal diffusivity of a material. The total thermal conductivity ( $\kappa_{tot}$ ) is calculated with:

$$\kappa_{tot} = DC_p\rho \quad (2 - 1)$$

Where  $D$  is the measured thermal diffusivity,  $\rho$  is the measured density and  $C_p$  is the specific heat capacity of the material. However, experimental determination of specific heat capacity at

high temperature of solid materials is usually unreliable due to high atomic anharmonicity.

Therefore, the Dulong–Petit law is used to predict the specific heat capacity of samples.

With the assistance from Dr. Yu-Chih Tseng, thermal diffusivity was measured on the NETZSCH LFA 457 Microflash instrument located at CanmetMATERIALS, Natural Resources of Canada, Hamilton, ON.

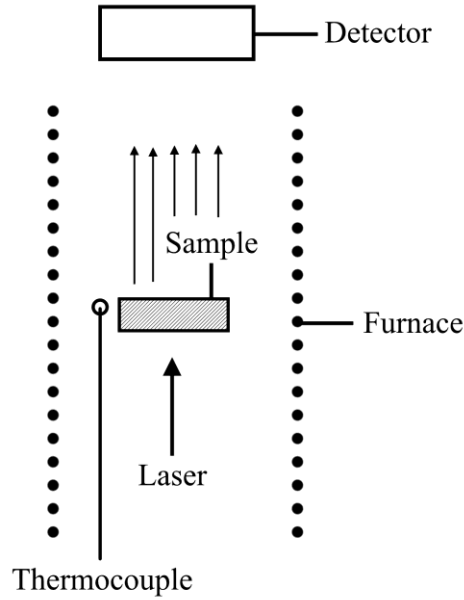


Figure 2.8. Schematics of the NETZSCH LFA 457 Microflash instrument.

Using the Dulong–Petit law and the Maier-Kelly polynomial <sup>44</sup>,  $C_p$  can be calculated:

$$C_p [Jg^{-1}K^{-1}] = \frac{3NR}{M_w} (1 + 1.3 \times 10^{-4} T - 4 \times 10^3 T^{-2}) \quad (2 - 2)$$

$N$  is the number of atoms per formula unit ( $Mg_3Sb_2$ ,  $N = 5$ ),  $R$  is the ideal gas constant, and  $M_w$  is the molecular weight of the sample.

## References

1. Chen, X., Wu, H., Cui, J., Xiao, Y., Zhang, Y., He, J., Chen, Y., Cao, J., Cai, W., Pennycook, S. J., Liu, Z., Zhao, L.-D., & Sui, J. (2018). Extraordinary thermoelectric performance in N-type manganese doped  $\text{Mg}_3\text{Sb}_2$  Zintl: High band degeneracy, tuned carrier scattering mechanism and hierarchical microstructure. *Nano Energy*, 52, 246–255. <https://doi.org/10.1016/j.nanoen.2018.07.059>
2. Guo, K., Cao, Q., Feng, X., Tang, M., Chen, H., Guo, X., Chen, L., Grin, Y., & Zhao, J. (2011). Enhanced thermoelectric figure of merit of zintl phase  $\text{YbCd}_2\text{-xMn}_x\text{Sb}_2$  by chemical substitution. *European Journal of Inorganic Chemistry*, 2011(26), 4043–4048. <https://doi.org/10.1002/ejic.201100282>
3. Tani, J., & Ishikawa, H. (2020). Thermoelectric properties of Te-doped  $\text{Mg}_3\text{Sb}_2$  synthesized by Spark Plasma Sintering. *Physica B: Condensed Matter*, 588, 412173. <https://doi.org/10.1016/j.physb.2020.412173>
4. Wang, Y., Zhang, X., Wang, Y., Liu, N., Liu, Y., & Lu, Q. (2022). High thermoelectric performance of nanostructured  $\text{Mg}_3\text{Sb}_2$  on synergistic te-doping and Mg/Y interstitial. *Journal of Materials Science*, 57(5), 3183–3192. <https://doi.org/10.1007/s10853-021-06797-y>
5. Phan, T., Tseng, Y.-C., & Mozharivskyj, Y. (2025). Optimization of thermoelectric properties of N-type mn- and te-doped  $\text{Mg}_3\text{Sb}_2\text{-Bi}$  phases. *Solid State Sciences*, 168, 108011. <https://doi.org/10.1016/j.solidstatesciences.2025.108011>
6. Zhang, J., Song, L., & Iversen, B. B. (2020). Probing efficient n-type lanthanide dopants for  $\text{mg}_3\text{sb}_2$  thermoelectrics. *Advanced Science*, 7(24). <https://doi.org/10.1002/advs.202002867>



7. Li, J., Zhang, S., Jia, F., Zheng, S., Shi, X., Jiang, D., Wang, S., Lu, G., Wu, L., & Chen, Z.-G. (2020). Point defect engineering and machinability in N-type  $\text{Mg}_3\text{Sb}_2$ -based materials. *Materials Today Physics*, 15, 100269.  
<https://doi.org/10.1016/j.mtphys.2020.100269>
8. Zhang, J., Song, L., & Iversen, B. B. (2021). Improved thermoelectric properties of N-type  $\text{Mg}_3\text{Sb}_2$  through cation-site doping with Gd or Ho. *ACS Applied Materials & Interfaces*, 13(9), 10964–10971. <https://doi.org/10.1021/acsami.0c22558>
9. Lei, J., Wuliji, H., Zhao, K., Wei, T.-R., Xu, Q., Li, P., Qiu, P., & Shi, X. (2021). Efficient lanthanide Gd doping promoting the thermoelectric performance of  $\text{Mg}_3\text{Sb}_2$ -based materials. *Journal of Materials Chemistry A*, 9(46), 25944–25953.  
<https://doi.org/10.1039/d1ta07988c>
10. Brown, S. R., Kauzlarich, S. M., Gascoin, F., & Snyder, G. J. (2006).  $\text{Yb}_{14}\text{MnSb}_{11}$ : new high efficiency thermoelectric material for power generation. *Chemistry of Materials*, 18(7), 1873–1877. <https://doi.org/10.1021/cm060261t>
11. Grebenkemper, J. H., Hu, Y., Barrett, D., Gogna, P., Huang, C.-K., Bux, S. K., & Kauzlarich, S. M. (2015). High temperature thermoelectric properties of  $\text{Yb}_{14}\text{MnSb}_{11}$  prepared from reaction of  $\text{MnSb}$  with the elements. *Chemistry of Materials*, 27(16), 5791–5798. <https://doi.org/10.1021/acs.chemmater.5b02446>
12. Gascoin, F., Ottensmann, S., Stark, D., Haïle, S. M., & Snyder, G. J. (2005). Zintl phases as thermoelectric materials: Tuned transport properties of the compounds  $\text{Ca}_{x}\text{Yb}_{1-x}\text{Zn}_2\text{Sb}_2$ . *Advanced Functional Materials*, 15(11), 1860–1864.  
<https://doi.org/10.1002/adfm.200500043>

13. Chanakian, S., Aydemir, U., Zevalkink, A., Gibbs, Z. M., Fleurial, J.-P., Bux, S., & Jeffrey Snyder, G. (2015). High temperature thermoelectric properties of zn-doped  $\text{Eu}_5\text{In}_2\text{Sb}_6$ . *Journal of Materials Chemistry C*, 3(40), 10518–10524.  
<https://doi.org/10.1039/c5tc01645b>
14. Shuai, J., Geng, H., Lan, Y., Zhu, Z., Wang, C., Liu, Z., Bao, J., Chu, C.-W., Sui, J., & Ren, Z. (2016). Higher thermoelectric performance of Zintl Phases  $(\text{Eu}_{0.5}\text{Yb}_{0.5})_1\text{-x}\text{Ca}_{\text{x}}\text{Mg}_2\text{Bi}_2$  by band engineering and strain fluctuation. *Proceedings of the National Academy of Sciences*, 113(29). <https://doi.org/10.1073/pnas.1608794113>
15. Bux, S. K., Zevalkink, A., Janka, O., Uhl, D., Kauzlarich, S., Snyder, J. G., & Fleurial, J.-P. (2014). Glass-like lattice thermal conductivity and high thermoelectric efficiency in  $\text{YB}_9\text{mn}_4.2\text{sb}_9$ . *J. Mater. Chem. A*, 2(1), 215–220. <https://doi.org/10.1039/c3ta14021k>
16. Price, S. (n.d.). The Peltier Effect and Thermoelectric Cooling. The peltier effect and thermoelectric cooling. [https://ffden-2.phys.uaf.edu/212\\_spring2007.web.dir/sedona\\_price/phys\\_212\\_webproj\\_peltier.html](https://ffden-2.phys.uaf.edu/212_spring2007.web.dir/sedona_price/phys_212_webproj_peltier.html)
17. Thomson, William (1857). "4. On a Mechanical Theory of Thermo-Electric Currents". *Proceedings of the Royal Society of Edinburgh*. 3. Cambridge Univ. Press: 91–98.  
doi:10.1017/S0370164600027310 (inactive 2024-11-11).
18. Christian, J. W., Templeton, I. M., Pearson, W. B., & Jan, J. (1958). Thermo-electricity at low temperatures. vi. A redetermination of the absolute scale of thermo-electric power of lead. *Proceedings of the Royal Society of London. Series A. Mathematical and Physical Sciences*, 245(1241), 213–221. <https://doi.org/10.1098/rspa.1958.0078>
19. Drude, P. (1900). *Zur Elektronentheorie der Metalle*. *Annalen Der Physik*, 306(3), 566–613. <https://doi.org/10.1002/andp.19003060312>

20. Drude, P. (1900b). Zur Elektronentheorie der Metalle; ii. Teil. Galvanomagnetische und thermomagnetische effecte. *Annalen Der Physik*, 308(11), 369–402.  
<https://doi.org/10.1002/andp.19003081102>
21. Peter Y. Yu; Manuel Cardona (30 May 2010). *Fundamentals of Semiconductors: Physics and Materials Properties*. Springer. pp. 205–. ISBN 978-3-642-00709-5.
22. Andrew F. May, G. Jeffery Snyder "Introduction to Modeling Thermoelectric Transport at High Temperatures" Chapter 11 in *Thermoelectrics and its Energy Harvesting Vol 1*, edited by D. M. Rowe. CRC Press (2012).
23. W. D. Callister and D. G. Rethwisch, "Materials Science and Engineering an Introduction," textbook, 8th Edition, Wiley, (2010).
24. L. Solymar and D. Walsh, "Electrical Properties of Materials," textbook, 7th Edition, Oxford Press, (2004).
25. R. E. Hummel, "Electronic Properties of Materials," textbook, 4th Edition, Springer, (2011).
26. R. E. Hummel, "Electronic Properties of Materials," textbook, 4th Edition, Springer, (2011).
27. Hyun Sik Kim, Zachary Gibbs, Yinglu Tang, Heng Wang, and G. J. Snyder "Characterization of Lorenz number with Seebeck coefficient measurement" *APL Materials* 3 041506 (2015).
28. Chen, C., Li, X., Li, S., Wang, X., Zhang, Z., Sui, J., Cao, F., Liu, X., & Zhang, Q. (2018). Enhanced thermoelectric performance of P-type  $\text{mg}_3\text{sb}_2$  by lithium doping and its tunability in an anionic framework. *Journal of Materials Science*, 53(23), 16001–16009. <https://doi.org/10.1007/s10853-018-2555-2>

29. Wang, H., Chen, J., Lu, T., Zhu, K., Li, S., Liu, J., & Zhao, H. (2018). Enhanced thermoelectric performance in P-type  $\text{Mg}_3\text{Sb}_2$  via lithium doping. *Chinese Physics B*, 27(4), 047212. <https://doi.org/10.1088/1674-1056/27/4/047212>
30. Shuai, J., Wang, Y., Kim, H. S., Liu, Z., Sun, J., Chen, S., Sui, J., & Ren, Z. (2015). Thermoelectric properties of Na-doped Zintl compound:  $\text{Mg}_3\text{-NA Sb}_2$ . *Acta Materialia*, 93, 187–193. <https://doi.org/10.1016/j.actamat.2015.04.023>
31. Ren, Z., Shuai, J., Mao, J., Zhu, Q., Song, S., Ni, Y., & Chen, S. (2018). Significantly enhanced thermoelectric properties of P-type  $\text{Mg}_3\text{Sb}_2$  via co-doping of Na and Zn. *Acta Materialia*, 143, 265–271. <https://doi.org/10.1016/j.actamat.2017.10.015>
32. Song, L., Zhang, J., & Iversen, B. B. (2017). Simultaneous improvement of power factor and thermal conductivity via Ag doping in P-type  $\text{Mg}_3\text{Sb}_2$  thermoelectric materials. *Journal of Materials Chemistry A*, 5(10), 4932–4939. <https://doi.org/10.1039/c6ta08316a>
33. Kannan, V. P., Lourdhusamy, V., Paulraj, I., Madanagurusamy, S., & Liu, C.-J. (2024). Significantly enhanced thermoelectric performance of p-type  $\text{Mg}_3\text{Sb}_2$  via Zn substitution on Mg(2) site: Optimization of hole concentration through Ag Doping. *ACS Applied Materials & Interfaces*, 16(43), 58677–58688. <https://doi.org/10.1021/acsami.4c12868>
34. Tiadi, M., Battabyal, M., Jain, P. K., Chauhan, A., Satapathy, D. K., & Gopalan, R. (2021). Enhancing the thermoelectric efficiency in P-type  $\text{Mg}_3\text{Sb}_2$  via Mg site co-doping. *Sustainable Energy & Fuels*, 5(16), 4104–4114. <https://doi.org/10.1039/d1se00656h>

35. Kong, D., Zhao, H., & Fan, X. (2024). Enhanced thermoelectric performance of a P-type  $\text{mg}_3\text{sb}_2$ -based Zintl phase compound via GE doping. *Journal of Solid State Chemistry*, 339, 124977. <https://doi.org/10.1016/j.jssc.2024.124977>
36. Bhardwaj, A., & Misra, D. K. (2014). Enhancing thermoelectric properties of a P-type  $\text{mg}_3\text{sb}_2$ - based Zintl phase compound by PB substitution in the anionic framework. *RSC Adv.*, 4(65), 34552–34560. <https://doi.org/10.1039/c4ra04889j>
37. Wang, Yang, Zhang, X., Liu, Y., Wang, Y., Zhang, J., & Yue, M. (2020). Optimizing the thermoelectric performance of P-type  $\text{mg}_3\text{sb}_2$  by SN Doping. *Vacuum*, 177, 109388. <https://doi.org/10.1016/j.vacuum.2020.109388>
38. Ahmadpour, F., Kolodiazhnyi, T., & Mozharivskyj, Y. (2007). Structural and physical properties of  $\text{mg}_{3-x}\text{zn}_x\text{sb}_2$  ( $x=0-1.34$ ). *Journal of Solid State Chemistry*, 180(9), 2420–2428. <https://doi.org/10.1016/j.jssc.2007.06.011>
39. Kannan, V. P., Lourdhusamy, V., Paulraj, I., Madanagurusamy, S., & Liu, C.-J. (2024). Significantly enhanced thermoelectric performance of p-type  $\text{mg}_3\text{sb}_2$  via zn substitution on Mg(2) site: Optimization of hole concentration through Ag Doping. *ACS Applied Materials & Interfaces*, 16(43), 58677–58688. <https://doi.org/10.1021/acsami.4c12868>
40. Ren, Z., Shuai, J., Mao, J., Zhu, Q., Song, S., Ni, Y., & Chen, S. (2018). Significantly enhanced thermoelectric properties of P-type  $\text{MG}_3\text{SB}_2$  via co-doping of Na and zn. *Acta Materialia*, 143, 265–271. <https://doi.org/10.1016/j.actamat.2017.10.015>
41. Tang, X., Zhang, B., Zhang, X., Wang, S., Lu, X., Han, G., Wang, G., & Zhou, X. (2020). Enhancing the thermoelectric performance of P-type  $\text{mg}_3\text{sb}_2$  via codoping of Li

and CD. ACS Applied Materials & Interfaces, 12(7), 8359–8365.

<https://doi.org/10.1021/acsami.9b23059>

42. Xiao, S., Peng, K., Zhou, Z., Wang, H., Zheng, S., Lu, X., Han, G., Wang, G., & Zhou, X. (2023). Realizing CD and ag codoping in P-type mg3sb2 toward high thermoelectric performance. Journal of Magnesium and Alloys, 11(7), 2486–2494.

<https://doi.org/10.1016/j.jma.2021.09.012>

43. Ratzker, B., & Sokol, M. (2023). Exploring the capabilities of high-pressure spark plasma sintering (HPSPS): A review of Materials Processing and properties. Materials & Design, 233, 112238. <https://doi.org/10.1016/j.matdes.2023.112238>

44. Agne, M. T., Imasato, K., Anand, S., Lee, K., Bux, S. K., Zevalkink, A., Rettie, A. J. E., Chung, D. Y., Kanatzidis, M. G., & Snyder, G. J. (2018). Heat capacity of MG3SB2, MG3BI2, and their alloys at high temperature. Materials Today Physics, 6, 83–88.

<https://doi.org/10.1016/j.mtphys.2018.10.001>

## Chapter 3. Thermoelectric studies of *p*-type Zn, Na and Ag doped Mg<sub>3</sub>Sb<sub>2</sub> based thermoelectric materials

### 3.1 Abstract

Near phase pure (>99 wt.%) Zn, Na and Ag doped *p*-type Mg<sub>3</sub>Sb<sub>2</sub> based compositions were synthesized. Due to heavier atomic substitution on the Mg site, the lattice thermal conductivity  $\kappa_L$  was expected to be lower compared to undoped Mg<sub>3</sub>Sb<sub>2</sub> via increased mass difference, that leads to reduced lattice vibration and increased phonon scattering. The thermoelectric properties of the samples were investigated; Na doping significantly increased electrical conductivity  $\sigma$ . However, the total thermal conductivity  $\kappa_{tot}$  also increases due to increased electronic component  $\kappa_e$ . Ag doping also increased electrical conductivity  $\sigma$ . However, due to band gap narrowing, Ag doped samples exhibit significant bipolar effect at higher temperatures. Using Wiedemann Franz' law, it was deduced that Ag-doped compositions have inferior charge carrier mobility  $\eta$  compared to Na-doped compositions, and this lead to superior  $\kappa_{tot}$  due to smaller  $\kappa_e$ .

### 3.2 Introduction

Zn substitution in Mg<sub>3</sub>Sb<sub>2</sub> based Zintl thermoelectric material was performed by Ahmadpour et al., 2007<sup>1</sup>. It was reported Zn doping narrows the band gap and increases electrical conductivity  $\sigma$  significantly when compared to pristine Mg<sub>3</sub>Sb<sub>2</sub>. The increased mass difference between Zn<sup>2+</sup> and Mg<sup>2+</sup> also significantly lowers lattice thermal conductivity  $\kappa_L$  due to increased phonon scattering. However, even with superior  $\sigma$  and  $\kappa$ , the Zn single doped materials

are still poor thermoelectric material due to their intrinsically low  $\sigma$ . Single *p*-type doping, such as with Li and Na, was attempted on  $\text{Mg}_3\text{Sb}_2$  <sup>2,3,4</sup> to increase its  $\sigma$ . With the superior thermoelectric properties of Zn doped  $\text{Mg}_3\text{Sb}_2$ , Zn/Na co-doping was performed by Ren et al., 2018. The authors reported a  $\sim 76\%$  increase in average  $zT$  value, and a peak  $ZT$  of 0.8 at 773 K was achieved for the composition  $\text{Zn}_{0.9}\text{Mg}_{2.075}\text{Na}_{0.0125}\text{Sb}_2$  <sup>5</sup>. Ag doping and Zn/Ag co-doping were investigated by Song et al., 2017 <sup>6</sup>, and Kannan et al., 2024 <sup>7</sup>, with both groups reporting that Ag doping increases both  $\sigma$  and  $\kappa$ , but results in undesirable bipolar effect at higher temperatures due to a narrow band gap.

In this section, the experimental reproduction of Zn/Na co-doping was attempted, but a non-traditional doping strategy was attempted by synthesizing a sodium antimonide ( $\text{NaSb}$ ) <sup>8</sup> precursor prior to ball milling due to the inability to ball mill soft Na metal. The effects of Zn, Na and Ag triple co-doping was also investigated.

### 3.3 Experimental

Na metal and, Sb (chunks, 99.999 wt.%, 5N Plus) were weighed stoichiometrically according to the 1:1 composition of  $\text{NaSb}$ . The weighed elements were then placed in a carbon coated quartz tube in an argon-filled glovebox. The carbon coated quartz tube is then vacuum sealed and placed inside of a furnace (Thermo Scientific Thermolyne Industrial Benchtop Muffle Furnaces), heated to 700 °C at a rate of 200 °C/h and annealed at 700 °C for two days. The tube was then quenched in ice cold water, dried and transferred back into the argon-filled glovebox. Needle-shaped, shiny crystalline sodium antimonide ( $\text{NaSb}$ ) was extracted from the ampoule. Elemental Mg (powder, 99 wt.%, Sigma-Aldrich), Sb (chunks, 99.999 wt.%, 5N Plus), Zn (99.995 wt.%, Sigma-Aldrich), Ag (99.9 wt.%, thermo scientific) as well as the precursor



material NaSb were weighed inside the argon-filled glovebox according to the composition  $\text{Zn}(\text{NaSb})_x\text{Ag}_y\text{Mg}_{2.05-x-y}\text{Sb}_{2-x}$  ( $x = 0, 0.015, 0.02, 0.03, y = 0, 0.02, 0.03$ ). A small amount of extra Mg (0.05 stoichiometric amount) was added to compensate for Mg loss during Spark Plasma Sintering due to its high vapor pressure. The mixture was then placed inside a stainless steel ball mill jar filled with several 10mm diameter stainless steel balls (the sample to balls weight ratio is 1:5) and capped with the air-tight lid in the glovebox. The sample in the jar was processed on a high energy ball mill (FRITZCH Planetary Mono Mill PULVERISETTE 6) for 5 hours at 400 RPM (Transmission ratio 1:1.82 relative to main disk). The obtained powder was then also grinded and mixed using an agate mortar and pastel to ensure homogenous mixing inside the glove box. The finely grounded powder was then transferred into 12.7mm and 14.7mm high density graphite dies inside the glovebox. The dies were transferred into a Spark Plasma Sintering chamber (DR. SINTER LAB Jr. SPS-211), sintered at 550 °C for 30 minutes under the applied pressure of 50 MPa until cool down. The consolidated pellets were polished with silicon carbide paper.

The 12.7mm consolidated pellet was cut in half; phase analysis was done on the PANalytical X'Pert powderdiffractometer (CoK $\alpha$  radiation, X'Celerator line detector), the microstructure and compositional EDS analyses were done TESCAN VEGA SEM. The Seebeck coefficient  $S$  and electrical conductivity  $\sigma$  were simultaneously measured on the NETZSCH SBA 458 Nemesis instrument using the 4-point method. The thermal diffusivity  $D$  was measured on the NETZSCH LFA 457 Microflash instrument and, density,  $\rho$ , was calculated from the experimental volume and mass (the pellet dimensions were measured with a caliper and weight on a 5-digit scale). The specific heat capacity  $C_p$  of the consolidated samples was estimated using

the Dulong–Petit law <sup>9</sup>. The thermal conductivity of the materials was calculated using the  $\kappa_{\text{tot}} = DC_p\rho$  equation.

### 3.4 Results and discussions

Pure  $\text{Mg}_3\text{Sb}_2$  is a *p*-type material. Intrinsic doping can be performed by changing the ratio between cation, Mg, and anion, Sb. To enhance its *p*-type behavior, the material must be electron deficient, which can be achieved by lowering the Mg content (this creates Mg vacancies). While formation of Mg vacancies is necessary for the *p*-type behavior, insufficient Mg amount will lead to impurities such as free Sb. In contrast, excessive Mg would prevent the formation of vacancies and lead to the *n*-type behavior.

$\text{Mg}_3\text{Sb}_2$  has a layered  $\text{Mn}_2\text{O}_3$ -type structure with the P-3m1 space group. One unit cell contains three Mg atoms and two Sb atoms – Mg atoms occupy two distinctive sites, a tetrahedral site and an octahedral site. Using the Crystal Field Stabilization Energy (CFSE) analysis, it can be concluded that Zn substitution in the Mg sites would not have a site preference,  $\text{Zn}^{2+}$  has a  $d^{10}$  configuration and no CFSE. However, multiple reports show the Zn substitution is site selective. Single X-Ray diffraction analysis shows that Zn tend to replace Mg on the tetrahedral site<sup>1,5</sup>. The Zn substitution increases phonon scattering, resulting in lower total thermal conductivity  $\kappa_{\text{tot}}$  <sup>1</sup>.

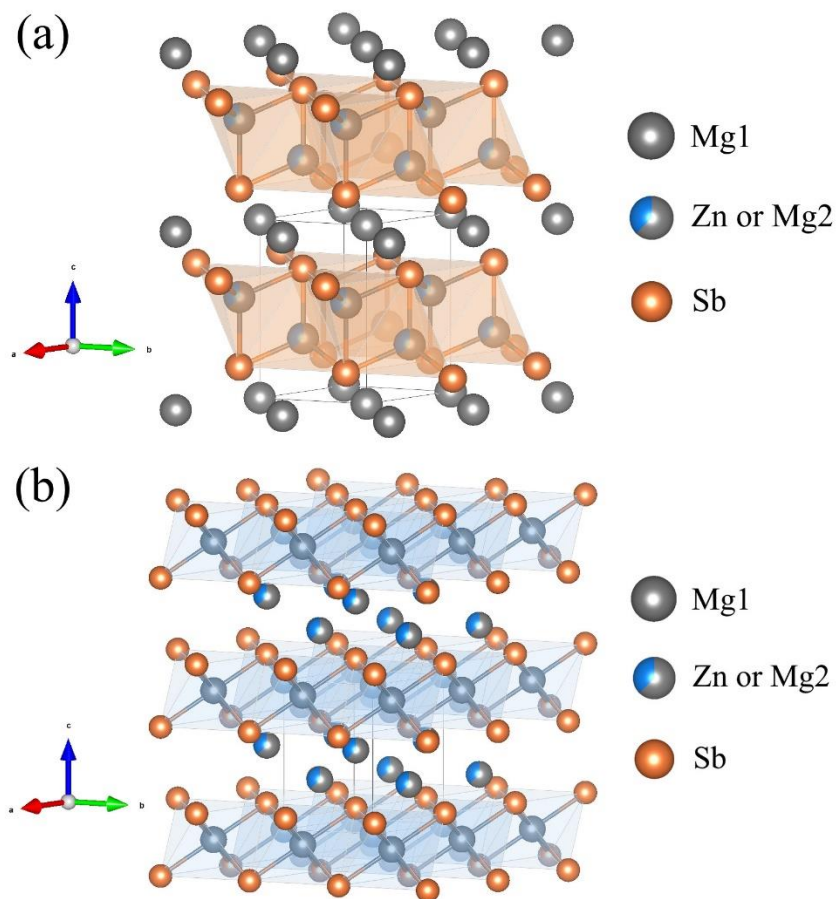


Figure 3.1. (a) Crystal structure of Zn substituted  $\text{Mg}_3\text{Sb}_2$ , indicating Zn atoms at the Mg2 position in the tetrahedral site. (b) Crystal structure indicating Mg1 surrounded by Sb octahedra.

In our study, the PXRD data showed that the high energy ball milled powders contain the  $\text{Mg}_3\text{Sb}_2$  main phase, and elemental Sb and Zn impurities. This suggests the duration of the milling time or the rotational speed of the planetary ball mill was insufficient. However, impurities almost disappeared and a near-phase pure sample was obtained after the SPS sintering. The PXRD results were supported by the SEM/EDS analysis.

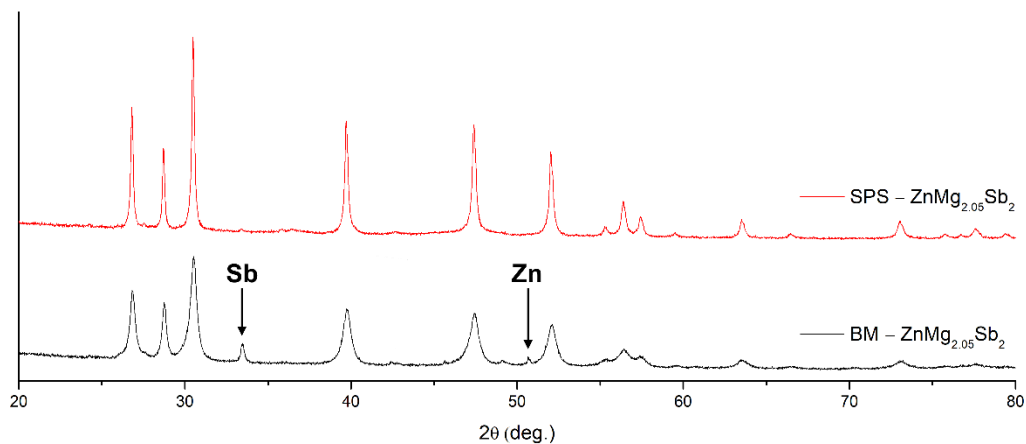
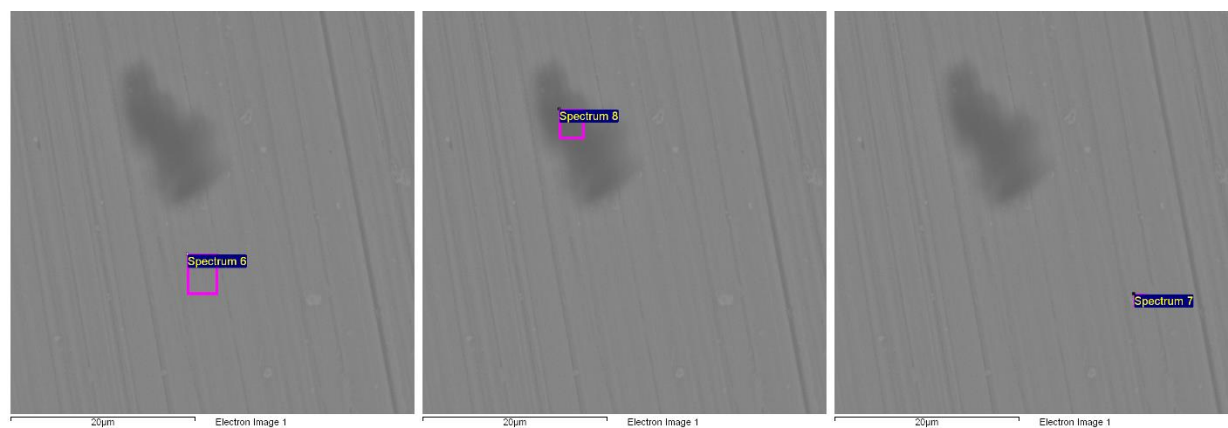


Figure 3.2. Powder x-ray diffraction pattern of ball milled (BM)  $\text{ZnMg}_{2.05}\text{Sb}_2$  indicating Sb and Zn impurity peaks and its sintered variant (SPS) indicating the absence of impurities.

Table 3.1. Rietveld refined phase analysis of BM –  $\text{ZnMg}_{2.05}\text{Sb}_2$  and SPS –  $\text{ZnMg}_{2.05}\text{Sb}_2$

| Sample                                   | Main phase (wt.%) | Sb (wt.%)       | Zn (wt.%)       |
|--|-------------------|-----------------|-----------------|
| Milled $\text{ZnMg}_{2.05}\text{Sb}_2$   | $94.03 \pm 0.43$  | $4.51 \pm 0.11$ | $1.47 \pm 0.08$ |
| Sintered $\text{ZnMg}_{2.05}\text{Sb}_2$ | $99.38 \pm 0.46$  | $0.62 \pm 0.09$ | -               |



| Element | Atomic% | Element | Atomic% | Element | Atomic% |
|---------|---------|---------|---------|---------|---------|
| Mg      | 40.36   | Mg      | 3.19    | Mg      | 21.46   |
| Zn      | 19.59   | Zn      | 1.97    | Zn      | 7.05    |
| Sb      | 40.05   | Sb      | 4.56    | Sb      | 52.67   |
| -       | -       | C       | 90.28   | Cr      | 3.35    |
| -       | -       | -       | -       | Fe      | 13.66   |

|   |   |   |   |    |      |
|---|---|---|---|----|------|
| - | - | - | - | Ni | 1.81 |
|---|---|---|---|----|------|

Table 3.2. SEM/EDS surface analysis of ZnMg<sub>2.05</sub>Sb<sub>2</sub>, showing main phase composition (left image & table) and contaminants (middle and right images & tables).

The SEM/EDS images of the three selected areas on the consolidated ZnMg<sub>2.05</sub>Sb<sub>2</sub> pellet show some amounts of Fe, Cr and Ni contamination, which likely come from the stainless-steel container and balls used for the high energy milling. An area with high C composition stems from the graphite punches used during the SPS.

### 3.4.1 PXRD and SEM/EDS phase analysis

Results of PXRD phase and EDS compositional analyses of the Zn and Na doped samples are compiled below. (See Supplementary Information for all PXRD and SEM/EDS results and images).

Table 3.3. PXRD phase analysis of Zn, Na/Ag doped sintered compositions

| Composition  | Main phase (wt.%) | Sb (wt.%)   |
|--|-------------------|-------------|
| ZnMg <sub>2.05</sub> Sb <sub>2</sub>                                       | 99.38 ± 0.46      | 0.62 ± 0.09 |
| ZnNa <sub>0.015</sub> Mg <sub>2.035</sub> Sb <sub>2</sub>                  | 99.96 ± 0.70      | 0.04 ± 0.12 |
| ZnNa <sub>0.03</sub> Mg <sub>2.02</sub> Sb <sub>2</sub>                    | 99.70 ± 0.42      | 0.30 ± 0.08 |
| ZnAg <sub>0.03</sub> Mg <sub>2.02</sub> Sb <sub>2</sub>                    | 99.80 ± 0.47      | 0.20 ± 0.08 |
| ZnAg <sub>0.02</sub> Na <sub>0.02</sub> Mg <sub>2.01</sub> Sb <sub>2</sub> | 99.87 ± 0.48      | 0.13 ± 0.08 |

Table 3.4. Rietveld refined PXRD parameters of Zn, Na/Ag doped sintered compositions

| Composition  | a = b     | c         | Cell volume<br>[Å <sup>3</sup> ] | Mw<br>[g/mol] | Theoretical<br>ρ [g/cm <sup>3</sup> ] |
|--|-----------|-----------|----------------------------------|---------------|---------------------------------------|
| ZnMg <sub>2.05</sub> Sb <sub>2</sub>                                       | 4.4484(2) | 7.2050(3) | 123.473(9)                       | 350.975       | 4.718                                 |
| ZnNa <sub>0.015</sub> Mg <sub>2.035</sub> Sb <sub>2</sub>                  | 4.4534(3) | 7.2079(5) | 123.80(1)                        | 345.609       | 4.634                                 |
| ZnNa <sub>0.03</sub> Mg <sub>2.02</sub> Sb <sub>2</sub>                    | 4.4537(2) | 7.2102(3) | 123.855(8)                       | 346.141       | 4.639                                 |
| ZnAg <sub>0.03</sub> Mg <sub>2.02</sub> Sb <sub>2</sub>                    | 4.4575(2) | 7.2064(4) | 124.00(1)                        | 342.982       | 4.591                                 |
| ZnAg <sub>0.02</sub> Na <sub>0.02</sub> Mg <sub>2.01</sub> Sb <sub>2</sub> | 4.4500(2) | 7.2087(3) | 123.620(8)                       | 347.214       | 4.662                                 |

|  |           |           |           |
|--|-----------|-----------|-----------|
| Mg <sub>3</sub> Sb <sub>2</sub> <sup>13</sup>  | 4.568(3)  | 7.229(4)  | 130.64    |
| Mg <sub>3</sub> Sb <sub>2</sub> (Experimental) | 4.5634(4) | 7.2337(7) | 130.46(2) |

Compared to the undoped Mg<sub>3</sub>Sb<sub>2</sub> with lattice constants  $a = b = 4.568(3)$ ,  $c = 7.229(4)$  Å and  $V_{\text{cell}} = 130.64$  [Å<sup>3</sup>] <sup>13</sup>, the Zn doped samples in this study have smaller lattice parameters due to smaller empirical atomic radius of Zn (Mg = 150pm, Zn = 135pm) <sup>27</sup>.

Table 3.5. EDS analysis of the Zn, Na/Ag doped SPS samples, indicating slight Zn deficiency.

| Composition  | Mg<br>(Atomic%) | Zn<br>(Atomic%) | Sb<br>(Atomic%) | Ag<br>(Atomic%) |
|--|-----------------|-----------------|-----------------|-----------------|
| ZnMg <sub>2.05</sub> Sb <sub>2</sub>                                       | 40.36           | 19.59           | 40.05           | -               |
| ZnNa <sub>0.015</sub> Mg <sub>2.035</sub> Sb <sub>2</sub>                  | 41.10           | 18.96           | 39.94           | -               |
| ZnNa <sub>0.03</sub> Mg <sub>2.02</sub> Sb <sub>2</sub>                    | 41.04           | 18.86           | 40.10           | -               |
| ZnAg <sub>0.03</sub> Mg <sub>2.02</sub> Sb <sub>2</sub>                    | 44.87           | 16.17           | 38.77           | 0.19            |
| ZnAg <sub>0.02</sub> Na <sub>0.02</sub> Mg <sub>2.01</sub> Sb <sub>2</sub> | 41.20           | 18.67           | 39.63           | 0.49            |

As evident from Table 3.5, all the SPS samples show slight Zn deficiency. As stated earlier, small excess Mg was added to account for Mg loss during sintering process due to the high vapor pressure of Mg. However, it was overlooked by us that Zn has an even higher vapor pressure compared to Mg <sup>10</sup>, and that leads to some Zn losses. If we were to repeat the experiments, we would also use some excess of Zn.

We could not reliably establish the Na concentration during the EDS analysis, since its emission line is close to the X-ray energy of Zn (Zn L $\alpha$  = 1.012keV vs Na K $\alpha$  = 1.041keV). Due to EDS signals overlap, the TESCAN VEGA peak integration would provide overestimation of the Na content (~5 to 15 at. %).

### 3.4.2 Electronic transport properties

The electronic transport properties, Seebeck coefficients,  $S$ , electrical conductivity,  $\sigma$ , and power factors, PF, of the three Zn/Na doped samples are shown in Figure 4. According to the experimental results, Na is a potent charge carrier dopant and the Na doped samples ( $x = 0.015$ ,  $0.03$  and  $x=0.02/y=0.02$ ) have significantly higher  $\sigma$  at all temperatures. All the Zn/Na doped samples behave similarly to a metal, as increasing temperature results in lower  $\sigma$ . While having high  $\sigma$ , the Na containing samples also have the lowest thermopower. As seen from Figure 4, all the samples except for the singly doped Zn composition have similar PF, and the PFs of  $\text{ZnNa}_{0.015}\text{Mg}_{2.035}\text{Sb}_2$  and  $\text{ZnAg}_{0.03}\text{Mg}_{2.02}\text{Sb}_2$  decreases above 600 K.

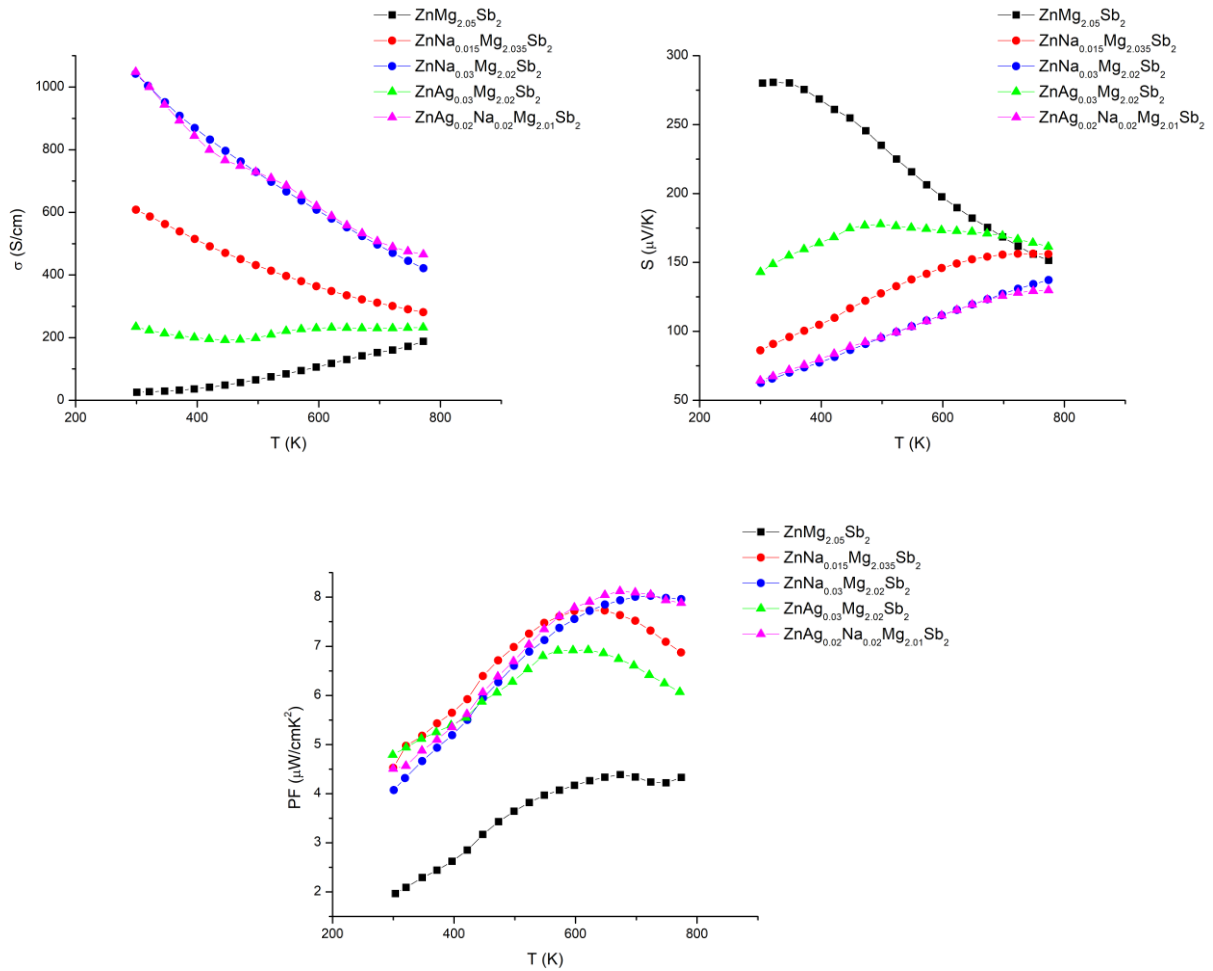


Figure 3.3. Temperature dependent electronic transport properties of  $\text{Zn}(\text{NaSb})_x\text{Ag}_y\text{Mg}_{2.05-x-y}\text{Sb}_2$  ( $x = 0, 0.015, 0.02, 0.03, y = 0, 0.02, 0.03$ ). Zn doped composition is plotted for comparison. There is a very noticeable inflection point at around 500 K on the electrical conductivity and Seebeck coefficient graph of the  $\text{ZnAg}_{0.03}\text{Mg}_{2.02}\text{Sb}_2$  sample: the  $\sigma$  increases slightly and S decreases with increasing temperature. This is due to Ag narrowing the band gap, which results in a bipolar effect.

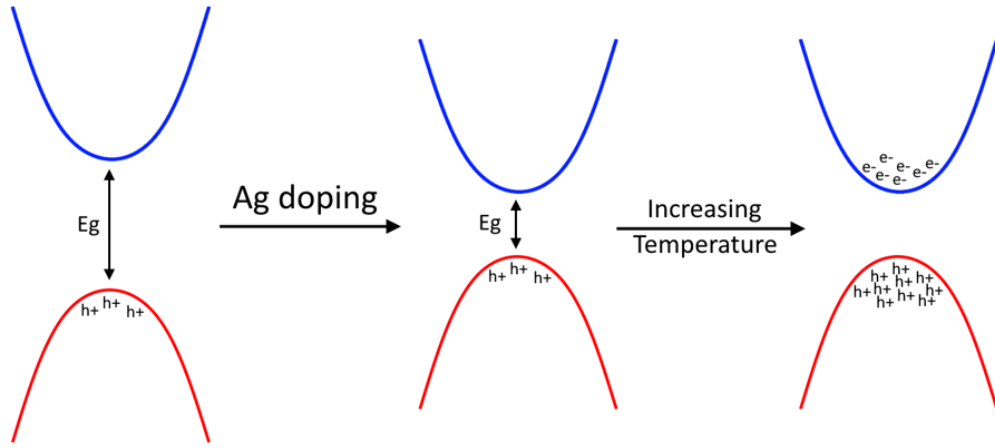


Figure 3.4. Graphical illustration of bipolar effect due to Ag doping. Ag narrows the band gap of the material, with increasing temperature both holes ( $h^+$ ) and electrons ( $e^-$ ) with opposite sign act as charge carriers.

$\sigma$  increases since both holes ( $h^+$ ) and electrons ( $e^-$ ) contribute to total measured electrical conductivity:

$$\sigma = \eta_h e |\mu_h| + \eta_e e |\mu_e|$$

$\eta$  is the charge carrier concentration,  $e$  is the charge per carrier and  $\mu$  is the carrier mobility.



The Seebeck coefficients, however, is reduced since the minority charge (electrons in this case) adds thermopower with the opposite sign ( $S_e < 0$ ). The holes, the major charge carriers, have a positive thermopower ( $S_h > 0$ ).

$$S = \frac{S_h \sigma_h + S_e \sigma_e}{\sigma_h + \sigma_e}$$

### 3.4.3 Thermal transport properties

Table 3.6. Compiled experimentally measured density and specific heat capacity estimated from the Dulong–Petit law. Calculated theoretical density = 4.89 g/cm<sup>3</sup> of Mg(Mg<sub>0.94</sub>Zn<sub>1.06</sub>)Sb<sub>2</sub> referenced from (Ahmadpour et al., 2007)<sup>1</sup>. Percent error represents difference between the theoretical and measured densities.

| Composition  | Measured $\rho$ [g/cm <sup>3</sup> ] | Relative $\rho$ | $C_p$ [J/gK] |
|--|--------------------------------------|-----------------|--------------|
| ZnMg <sub>2.05</sub> Sb <sub>2</sub>                                       | 4.62                                 | 94.48%          | 0.348        |
| ZnNa <sub>0.015</sub> Mg <sub>2.035</sub> Sb <sub>2</sub>                  | 4.66                                 | 95.30%          | 0.346        |
| ZnNa <sub>0.03</sub> Mg <sub>2.02</sub> Sb <sub>2</sub>                    | 4.58                                 | 93.66%          | 0.344        |
| ZnAg <sub>0.03</sub> Mg <sub>2.02</sub> Sb <sub>2</sub>                    | 4.70                                 | 96.11%          | 0.345        |
| ZnAg <sub>0.02</sub> Na <sub>0.02</sub> Mg <sub>2.01</sub> Sb <sub>2</sub> | 4.77                                 | 97.55%          | 0.346        |

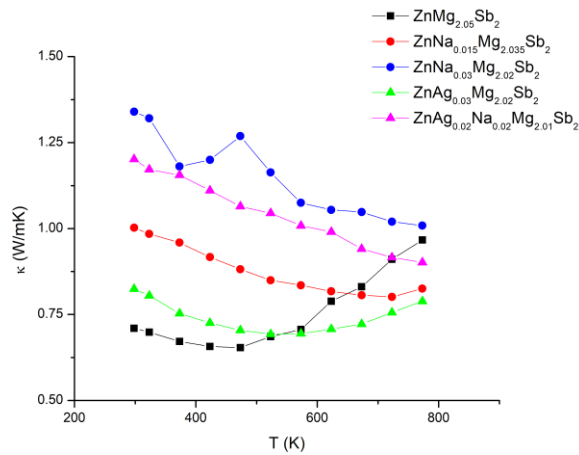


Figure 3.5. Thermal conductivity of Zn(NaSb)<sub>x</sub>Ag<sub>y</sub>Mg<sub>2.05-x-y</sub>Sb<sub>2-x</sub> ( $x = 0, 0.015, 0.02, 0.03, y = 0, 0.02, 0.03$ ).

The  $\kappa_{\text{tot}}$  of the samples was calculated from the measured density  $\rho$ , estimated specific heat capacity  $C_p$  and measured thermal diffusivity  $D$ . The samples with the highest measured  $\sigma$  also exhibit the highest  $\kappa$ . The electronic component of the thermal conductivity can be calculated using the Wiedemann-Franz's law:

$$\kappa_e = L\sigma T, \quad \sigma = \eta e \mu$$

$$\therefore \kappa_e = L(\eta e \mu)T$$

A fair comparison would be between the Na = 0.03 and Ag = 0.03 samples. Both materials have the same molar amounts of dopants and should have the same charge carrier density. However, the Na = 0.03 sample has a significantly higher  $\sigma$  likely due to higher carrier mobility ( $\mu_{\text{Na}0.03} > \mu_{\text{Ag}0.03}$ ). As a result,  $\sigma_{\text{Na}0.03} > \sigma_{\text{Ag}0.03}$ , and therefore  $\kappa_{\text{eNa}0.03} > \kappa_{\text{eAg}0.03}$ .

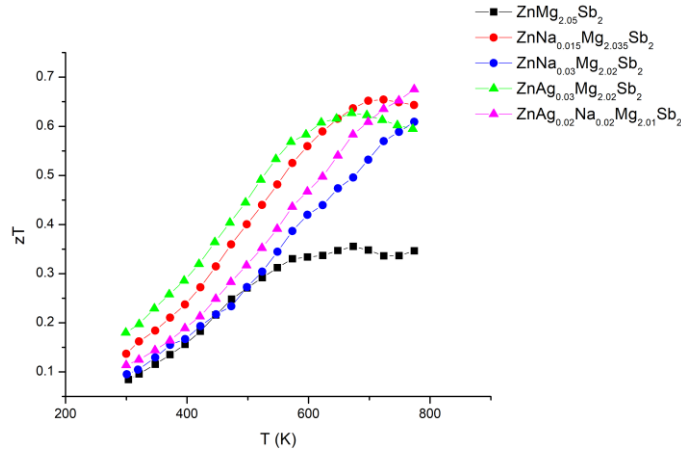


Figure 3.6.  $zT$  values of  $\text{Zn}(\text{NaSb})_x\text{Ag}_y\text{Mg}_{2.05-x-y}\text{Sb}_{2-x}$  ( $x = 0, 0.015, 0.02, 0.03, y = 0, 0.02, 0.03$ ).

The  $zT$  values in Figure 3.7 were calculated from the measured  $\sigma$ ,  $S$  and  $\kappa_{\text{tot}}$ :

$$zT = \frac{S^2 \sigma T}{\kappa}$$

The significant bipolar effect observed in the Ag = 0.03 sample results in the decrease of  $zT$  value at higher temperatures. The bipolar effect is also slightly observed in the Na = 0.015

sample at approximately 700 K. Despite  $\text{ZnNa}_{0.03}\text{Mg}_{2.02}\text{Sb}_2$  and  $\text{ZnAg}_{0.02}\text{Na}_{0.02}\text{Mg}_{2.01}\text{Sb}_2$  exhibiting the highest average PF, they also exhibit the highest  $\kappa_{\text{tot}}$  which results in lower zT values compared to the other samples (except Zn singly doped sample).

### 3.5 Conclusions

The isoelectronic Zn doping of  $\text{Mg}_3\text{Sb}_2$  is known to increase the material  $\sigma$  by narrowing the band gap and weakening its polar covalent bonding<sup>5, 11, 12</sup>. Our data show that all Zn doped samples exhibited metallic behavior, supporting this argument. The introduced mass difference between Zn and Mg lowers the  $\kappa$  of the material by increased lattice phonon scattering. The smaller size of substituted  $\text{Zn}^{2+}$  reduces the lattice parameters.  $\text{Na}^+$  doping increased the material's conductivity significantly and Na acts as a potent *p*-type charge carrier dopant.  $\text{Ag}^+$  also increased  $\sigma$ , but the carrier mobility of the Ag doped sample is inferior to that of the Na doped ones. Ag doping further narrowed the band gap, resulted in undesirable bipolar effect at high temperatures. The Ag = 0.03 doped composition ( $\text{ZnAg}_{0.03}\text{Mg}_{2.02}\text{Sb}_2$ ) exhibited the lowest  $\kappa_{\text{tot}}$ . Samples with high  $\sigma$  ( $\text{ZnNa}_{0.03}\text{Mg}_{2.02}\text{Sb}_2$  and  $\text{ZnAg}_{0.02}\text{Na}_{0.02}\text{Mg}_{2.01}\text{Sb}_2$ ) in this study also exhibited high  $\kappa$  due to the increased electronic component  $\kappa_e$ , resulting in lower zT values. Despite having lower  $\sigma$  compared to other samples,  $\text{ZnNa}_{0.015}\text{Mg}_{2.035}\text{Sb}_2$  and  $\text{ZnAg}_{0.03}\text{Mg}_{2.02}\text{Sb}_2$  have higher average zT values due to significantly lower  $\kappa_{\text{tot}}$ .

## Chapter 4. Thermoelectric studies of *p*-type Cd and Na co-doped Mg<sub>3</sub>Sb<sub>2</sub> based materials

### 4.1 Abstract

The high vapor pressure and relatively low melting point of Cd posed a significant challenge in synthesizing pure Cd-doped Mg<sub>3</sub>Sb<sub>2</sub> thermoelectric materials. All the Cd-doped samples decomposed at high temperatures and Cd vapors damaged the sample stage of the SBA 458 Nemesis instrument by forming brown cadmium oxide CdO. Due to the safety concerns associated with toxicity of CdO (CdO could be lethal at high amounts), only two Cd containing samples were studied.

### 4.2 Introduction

Cd/Li and Cd/Ag co-doped Mg<sub>3</sub>Sb<sub>2</sub> were reported by Tang et al., 2020<sup>14</sup> and Xiao et al., 2023<sup>15</sup>. However, the Cd/Na co-doped Mg<sub>3</sub>Sb<sub>2</sub> materials have never been reported. Similar to Zn doping, isoelectronic Cd<sup>2+</sup> substitution on Mg<sup>2+</sup> sites should decrease  $\kappa_L$  due to its significantly higher atomic mass, introducing mass-difference phonon scattering. Addition of Na, which was proven to be a potent *p*-type carrier dopant, should increase  $\sigma$  of the material similar to the Li doping. In this section, Cd and Na co-doping was attempted.

### 4.3 Experimental

Elemental Mg (powder, 99 wt.%, Sigma-Aldrich), Sb (chunks, 99.999 wt.%, 5N Plus), Cd (99.5 wt.%, Thermo Scientific) as well as the precursor material NaSb (its synthesis is

described in Chapter 3) were weighed inside of an argon-filled glovebox stoichiometrically according to the composition  $\text{Cd}(\text{NaSb})_x\text{Mg}_{2.05-x}\text{Sb}_{2-x}$  ( $x = 0, 0.03$ ). The mixtures were then ball milled and subjected to Spark Plasma Sintering at 823 K for 30 minutes. The ball milled powders and SPS consolidated samples were analyzed with PXRD and EDS. The electronic transport properties were measured on the SPS pellets.

Please refer to *Chapter 3, Section 3.3 Experimental* for detailed experimental procedures. The majority of the experimental procedures in this thesis follow the same protocol with the exception of starting materials and SPS temperatures.

## 4.4 Results and discussions

Due to the  $d^{10}$  configuration and inactivity of d-orbitals, cadmium atoms prefer tetrahedral environment as in tetragonal<sup>17, 18, 19</sup> or cubic, indicative of the  $sp^3$  hybridization (Tetragonal). However, when in the  $\text{Mg}_3\text{Sb}_2$  structure with two distinctive Mg sites, Cd may enter the larger octahedral site instead of smaller tetrahedral one. Thus, single crystal analysis on  $\text{CdMg}_2\text{Sb}_2$  would need to be performed to establish Cd site preference.

#### 4.4.1 PXRD and SEM/EDS phase analysis

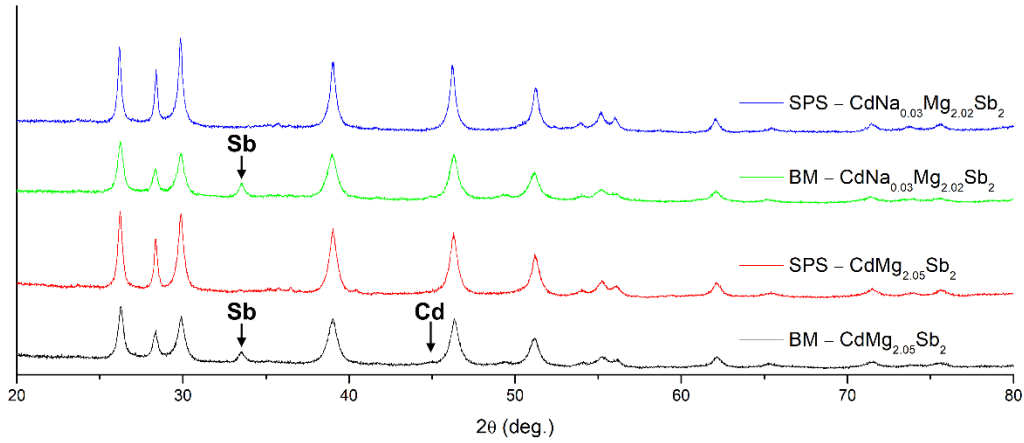


Figure 4.1. X-ray powder diffraction patterns of ball milled (BM) and sintered (SPS)

$\text{CdNa}_x\text{Mg}_{2.05-x}\text{Sb}_2$  ( $x = 0, 0.03$ ) samples

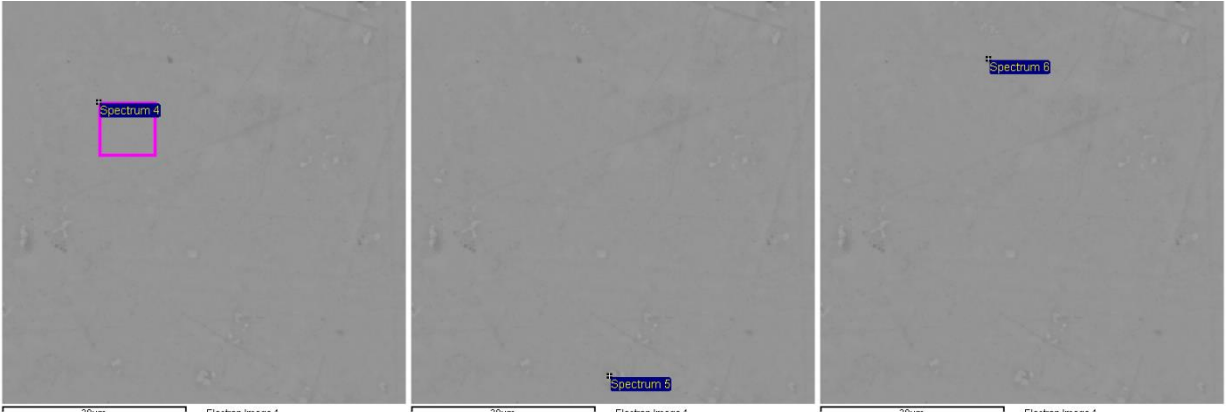
Table 4.1 Rietveld refined PXRD phase analysis of ball milled (BM) and sintered (SPS)  $\text{CdNa}_x\text{Mg}_{2.05-x}\text{Sb}_2$  ( $x = 0, 0.03$ ) compositions

| Composition   | Main phase (wt.%) | Sb (wt.%)       | Cd (wt.%)       |
|---|-------------------|-----------------|-----------------|
| BM – $\text{CdMg}_{2.05}\text{Sb}_2$                  | $94.93 \pm 0.65$  | $4.85 \pm 0.15$ | $0.22 \pm 0.05$ |
| SPS – $\text{CdMg}_{2.05}\text{Sb}_2$                 | $99.19 \pm 0.63$  | $0.62 \pm 0.11$ | $0.18 \pm 0.04$ |
| BM – $\text{CdNa}_{0.03}\text{Mg}_{2.05}\text{Sb}_2$  | $93.61 \pm 0.60$  | $6.29 \pm 0.14$ | $0.10 \pm 0.04$ |
| SPS – $\text{CdNa}_{0.03}\text{Mg}_{2.05}\text{Sb}_2$ | 100.00            | -               | -               |

Table 4.2. Rietveld refined lattice parameters of  $\text{CdNa}_x\text{Mg}_{2.05-x}\text{Sb}_2$  ( $x = 0, 0.03$ ) samples.  $\text{ZnMg}_{2.05}\text{Sb}_2$  is added for comparison, showing noticeable differences between Zn and Cd doped compositions.

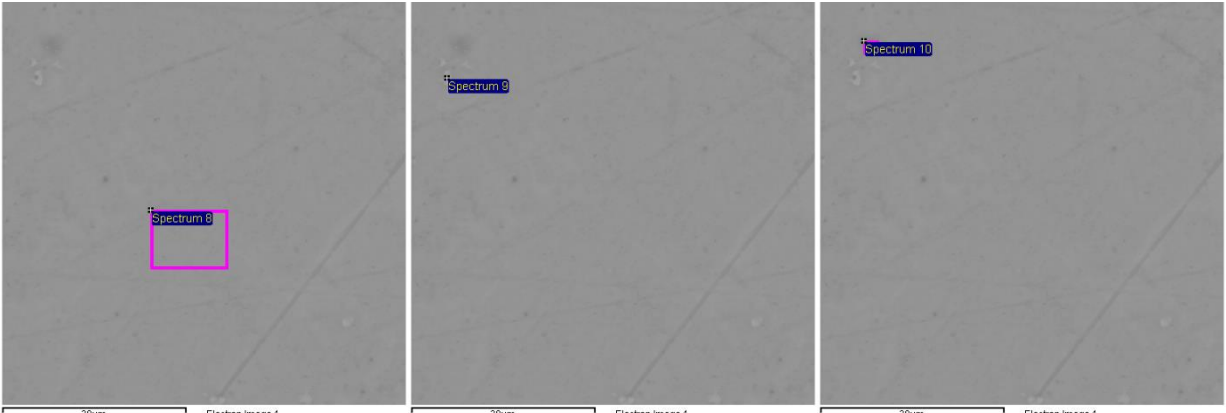
| Composition                                     | a = b     | c         | Cell volume [ $\text{\AA}^3$ ] |
|---|-----------|-----------|--------------------------------|
| $\text{ZnMg}_{2.05}\text{Sb}_2$                 | 4.4484(2) | 7.2050(3) | 123.47(9)                      |
| $\text{CdMg}_{2.05}\text{Sb}_2$                 | 4.5513(5) | 7.2973(8) | 130.91(2)                      |
| $\text{CdNa}_{0.03}\text{Mg}_{2.05}\text{Sb}_2$ | 4.5561(4) | 7.2894(7) | 131.04(2)                      |

Similar to the Zn doped samples, there were elemental Cd and Sb prior to SPS. After SPS, the amount of impurities significantly decreased. The EDS analysis of both Cd doped and Cd/Na co-doped samples revealed significant deviation from the targeted compositions.



| Element | Atomic% | Element | Atomic% | Element | Atomic% |
|---------|---------|---------|---------|---------|---------|
| Mg      | 48.69   | Mg      | 23.90   | Mg      | 39.88   |
| Cd      | 14.74   | Cd      | 6.48    | Cd      | 12.60   |
| Sb      | 36.56   | Sb      | 40.15   | Sb      | 30.99   |
| -       | -       | Cr      | 4.47    | Cr      | 0.52    |
| -       | -       | Fe      | 23.34   | Fe      | 4.18    |
| -       | -       | Ni      | 1.66    | Si      | 11.83   |

Table 4.3. EDS analysis of the SPS  $\text{CdMg}_{2.05}\text{Sb}_2$  pellet, indicating main phase with cadmium deficiency (left), steel contamination (middle) and silicon contamination, likely from residual sand from cleaning procedures of ball milling (right).



| Element | Atomic% | Element | Atomic% | Element | Atomic% |
|---------|---------|---------|---------|---------|---------|
| Na      | 0.36    | Mg      | 28.50   | Na      | 0.14    |
| Mg      | 51.17   | Cd      | 5.30    | Mg      | 20.67   |
| Cd      | 12.04   | Sb      | 37.69   | Cd      | 5.38    |
| Sb      | 36.43   | Cr      | 3.19    | Sb      | 15.85   |
| -       | -       | Fe      | 22.54   | C       | 57.96   |
| -       | -       | Ni      | 1.08    | -       | -       |
| -       | -       | Si      | 1.71    | -       | -       |

Table 4.4. EDS analysis of the SPS  $\text{CdMg}_{2.02}\text{Na}_{0.03}\text{Sb}_2$  pellet, indicating main phase with cadmium deficiency (left), steel contamination (middle) and carbon contamination (right).

According to the EDS results, the targeted  $\text{CdMg}_{2.05}\text{Sb}_2$  composition yielded  $\text{Cd}_{0.74}\text{Mg}_{2.46}\text{Sb}_{1.85}$ ; and  $\text{CdMg}_{2.02}\text{Na}_{0.03}\text{Sb}_2$  yielded  $\text{Cd}_{0.61}\text{Mg}_{2.58}\text{Na}_{0.018}\text{Sb}_{1.84}$ . EDS analysis showed significant deficiencies in Cd and Sb, and enrichment in Mg rich. The effects of high vapor pressure of Cd was not considered during the experimental design; a substantial amount of Cd was deposited on the walls inside of the SPS chamber during sintering (Supplementary Information). Both compositions were expected to exhibit *n*-type behavior due to excessive cation (Mg rich) and reduced anion content (Sb poor). However, the measured Seebeck coefficients *S* from the SBA 458 Nemesis were positive, indicating a *p*-type behavior.



#### 4.4.2 Electronic transport properties

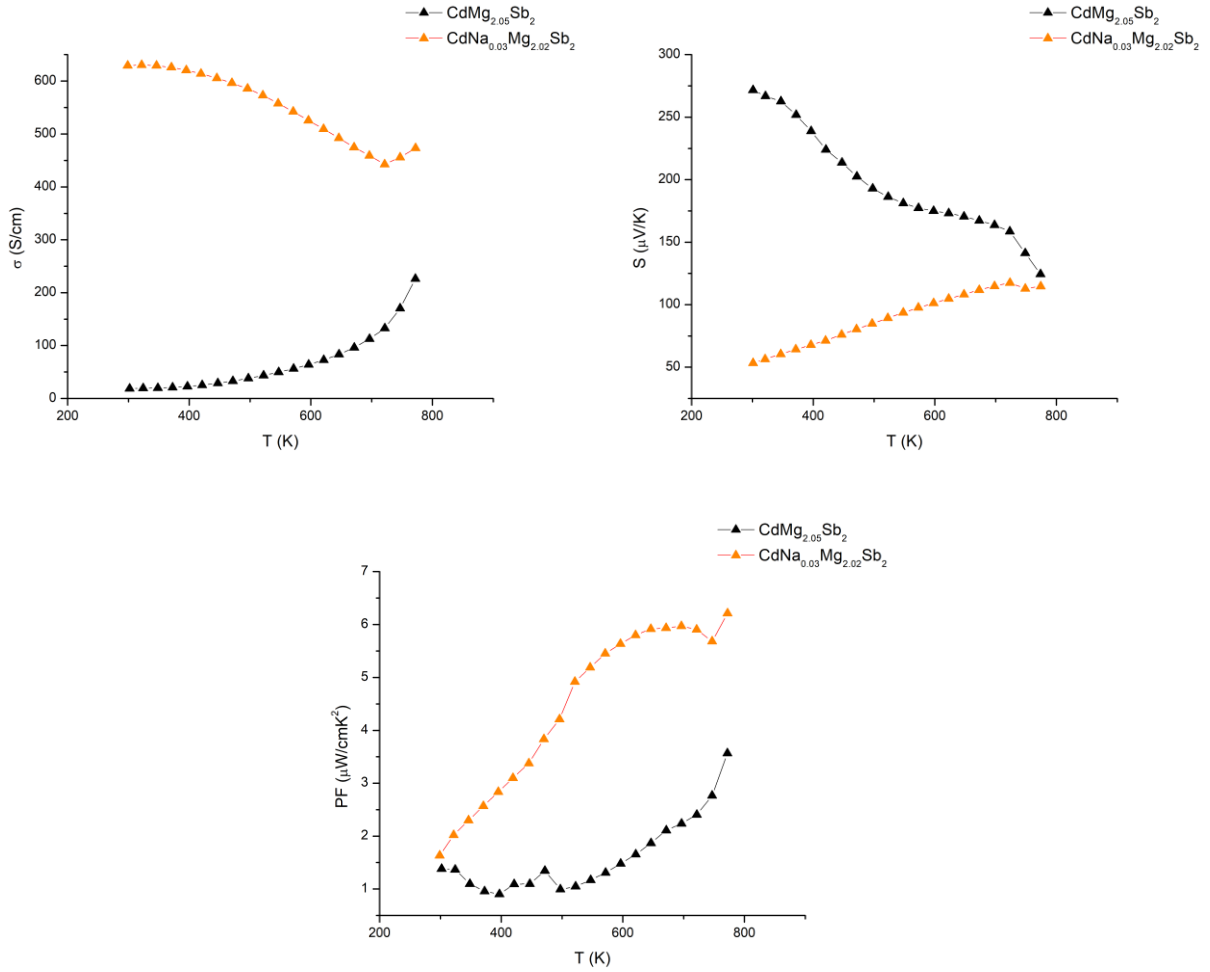


Figure 4.2. Temperature dependent electronic transport properties of  $\text{CdMg}_{2.05}\text{Sb}_2$  and  $\text{CdNa}_{0.03}\text{Mg}_{2.02}\text{Sb}_2$ .

The charge transport properties of the Cd doped and Cd/Na co-doped samples are shown in Figure 4.2. Despite significant Cd loss during sintering, the addition of Na has noticeably increased the electrical conductivity but lowered the thermopower. The Na doped sample  $\text{CdNa}_{0.03}\text{Mg}_{2.02}\text{Sb}_2$  exhibited much higher PF compared to  $\text{CdMg}_{2.02}\text{Sb}_2$ .

#### 4.4.3 Thermal decomposition of Cd doped $\text{Mg}_3\text{Sb}_2$

Unfortunately, both samples decomposed at high temperatures, as discovered after the property measurements (Figures S1.3a and S1.3b in the Supplementary Information). Brown deposits suggest cadmium oxide ( $\text{CdO}$ ). The sample stage of the NETZSCH SBA 458 Nemesis is made of alumina and silica, and the Cd vapors attacked the sample stage, forming brown cadmium oxide. The black circular deposits were due to previous samples attacking the sample stage.

Tang et al. and Xiao et al. co-doped  $\text{Mg}_3\text{Sb}_2$  with Cd/Li and Cd/Ag. However, the groups did not encounter problems with sample decomposition during high temperatures. The main difference between their study and our work is ball milling procedure. Both groups performed high energy ball milling (SPEX 8000 Mixer/Mill) for 10 hours, whereas this study used 5 hours (Planetary Mono Mill PULVERISETTE 6, 400 RPM). Although both groups did not specify the RPM of ball milling, it is assumed a higher “energy” ball milling was achieved due to the hardware specifications of SPEX 8000 Mill. It has fixed clamp and motor rotational speed, lowest at 1425 RPM motor speed and 875 cycles/minute<sup>21</sup>. Another experimental difference is the SPS duration and pressure. Tang et al. performed SPS at 973K for 30 minutes under 80 MPa; Xiao et al performed SPS at 873K for 20 minutes under 70 MPa. This study performed SPS at 823K for 30 minutes under 50 MPa.

It is unlikely the ball milling procedure is connected to the thermal decomposition of the Cd doped  $\text{Mg}_3\text{Sb}_2$  samples, since the PXRD phase analysis of ball milled samples show mainly unreacted Sb impurities. The Cd deposits inside the SPS chamber indicates decomposition during sintering at 823K, which is the lowest sintering temperature compared to the two studies. The relatively low pressure 50 MPa applied during our sintering may be the reason such

discrepancy occurred. Lower pressure during sintering may contribute to the insufficient densification of the material; high sintering pressure is usually used for thermally unstable materials<sup>22, 23, 24</sup>.

Since we did not see such decomposition behavior with other dopants, it is safe to say that the Cd doped  $\text{Mg}_3\text{Sb}_2$  samples are thermally unstable.

## 4.5 Conclusions

Due to safety concerns, the thermal transport properties measurements were not performed. Na is experimentally proven to be an excellent *p*-type carrier dopant again. Similar to Zn doping in Chapter 3, the planetary ball milling procedure failed to complete the synthesis, resulting in free Sb impurity. The high vapor pressure of Cd and associated Cd losses pose significant challenge in synthesizing target compositions. It is unclear whether the relatively low sintering pressure is connected to the thermal decomposition of Cd doped samples at high temperatures. In summary, more experimental data is needed to reach a sensible conclusion on Cd/Na doped  $\text{Mg}_3\text{Sb}_2$  materials.

## **Chapter 5. Failure of Zn/K co-doping in *p*-type Mg<sub>3</sub>Sb<sub>2</sub> based thermoelectric material**

### **5.1 Abstract**

It appears that K could not be co-doped with Zn into Mg<sub>3</sub>Sb<sub>2</sub> as there were no significant changes in measured thermoelectric properties.

### **5.2 Introduction**

Group I alkali metals such as Li and Na were reported by multiple groups as effective *p*-type dopant in Mg<sub>3</sub>Sb<sub>2</sub>, but there are no reports on K doping. Considering the existence of ternary alkaline earth containing compounds such as CaMg<sub>2</sub>Sb<sub>2</sub>, SrMg<sub>2</sub>Sb<sub>2</sub> and notably BaMg<sub>2</sub>Bi<sub>2</sub><sup>25</sup>, one can assume the possibility of K doping into Mg<sub>3</sub>Sb<sub>2</sub> (the ionic size of K<sup>+</sup>, 138 pm, is similar to that of Ba<sup>2+</sup>, 135 pm). The Zn/K co-doping followed the procedure similar to the Zn/Na co-doping in Chapter 3, and the potassium antimonide (KSb) precursor was prepared.

### **5.3 Experimental**

Elemental K (chunk, 99.95 wt.%, Thermo Scientific) and Sb (chunks, 99.999 wt.%, 5N Plus) were weighed according to the 1:1 composition KSb and then placed in a carbon coated quartz tube in an argon-filled glovebox. The carbon coated quartz tube is then vacuum sealed and heated to 650 °C at a rate of 150 °C/h and annealed at 650 °C for two days in Thermo Scientific Thermolyne Industrial Benchtop Muffle Furnaces). The tube was then quenched in ice cold water, dried and transferred back into the argon-filled glovebox. Chunky, shiny crystalline

potassium antimonide (KSb) was extracted from the ampoule. Elemental Mg (powder, 99 wt.%, Sigma-Aldrich), Sb (chunks, 99.999 wt.%, 5N Plus), Zn (99.995 wt.%, Sigma-Aldrich) as well as the precursor material KSb, was weighed inside an argon-filled glovebox according to the composition  $\text{Zn}(\text{KSb})_x\text{Mg}_{2.05-x}\text{Sb}_{2-x}$  ( $x = 0, 0.03$ ). The mixtures were then ball milled and spark plasma sintered at 823 K for 30 minutes under 50 MPa. The ball milled powders and consolidated pellets were analyzed with PXRD and SEM/EDS. The electronic transport properties were also measured.

Please refer to *Chapter 3, Section 3.3 Experimental* for detailed experimental procedures. The majority of the experimental procedures in this section follow the same protocol with the exception of starting materials and SPS temperature.

## 5.4 Results and discussions

Given a small amount of the K dopant, PXRD analysis will not be precise enough to establish the K presence by refining the lattice parameters. The EDS analysis is also unreliable due to a  $\pm 1\%$  integration errors ( $K = 0.03$ ,  $\sim 0.6\%$  atomic percent). Presence of K in the structure can be established from the charge transport property measurements. Similar to the Li and Na doping, a significant change in electrical conductivity is expected.

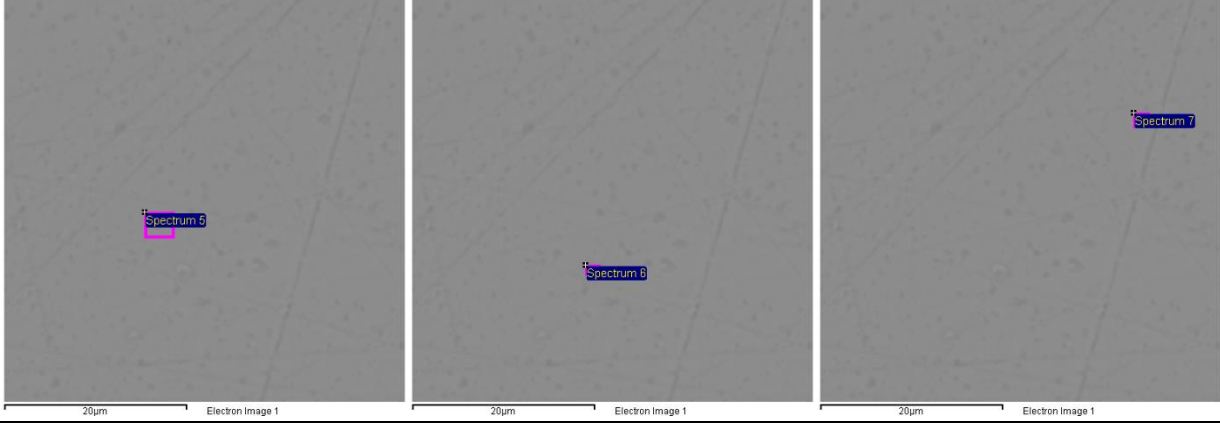
### 5.4.1 PXRD and SEM/EDS phase analysis

Table 5.1. Rietveld refined PXRD phase composition, indicating near pure main phase wt.%.

| Composition  | Main phase (wt.%) | Sb (wt.%)   |
|--|-------------------|-------------|
| ZnK <sub>0.03</sub> Mg <sub>2.02</sub> Sb <sub>2</sub> | 99.65 ± 0.50      | 0.35 ± 0.07 |

Table 5.2. Rietveld refined PXRD lattice parameters, indicating no significant difference between Zn/K co-doped composition and Zn single doped composition.

| Composition  | $a = b$ , Å | $c$ , Å   | Cell volume [Å <sup>3</sup> ] |
|--|-------------|-----------|-------------------------------|
| ZnMg <sub>2.05</sub> Sb <sub>2</sub>                   | 4.4484(2)   | 7.2050(3) | 123.47(9)                     |
| ZnK <sub>0.03</sub> Mg <sub>2.05</sub> Sb <sub>2</sub> | 4.4474(2)   | 7.2050(3) | 123.42(9)                     |



| Element | Atomic% | Element | Atomic% | Element | Atomic% |
|---------|---------|---------|---------|---------|---------|
| K       | 0.37    | Mg      | 29.12   | K       | 3.33    |
| Mg      | 40.73   | Zn      | 20.61   | Mg      | 40.62   |
| Zn      | 19.06   | Sb      | 36.64   | Zn      | 16.35   |
| Sb      | 39.84   | Cr      | 2.42    | Sb      | 39.70   |
| -       | -       | Fe      | 10.52   | -       | -       |
| -       | -       | Ni      | 0.69    | -       | -       |

Table 5.3. SEM/EDS analysis on the sintered ZnK<sub>0.03</sub>Mg<sub>2.02</sub>Sb<sub>2</sub> pellet, confirming the presence of K in the sample.

### 5.4.2 Electronic transport properties

Disappointingly, there were no significant changes in the charge transport properties after the K doping. Transport properties of ZnMg<sub>2.05</sub>Sb<sub>2</sub> and ZnK<sub>0.03</sub>Mg<sub>2.02</sub>Sb<sub>2</sub> are shown in Figure 5.1.; ZnNa<sub>0.03</sub>Mg<sub>2.02</sub>Sb<sub>2</sub> is added for comparison.

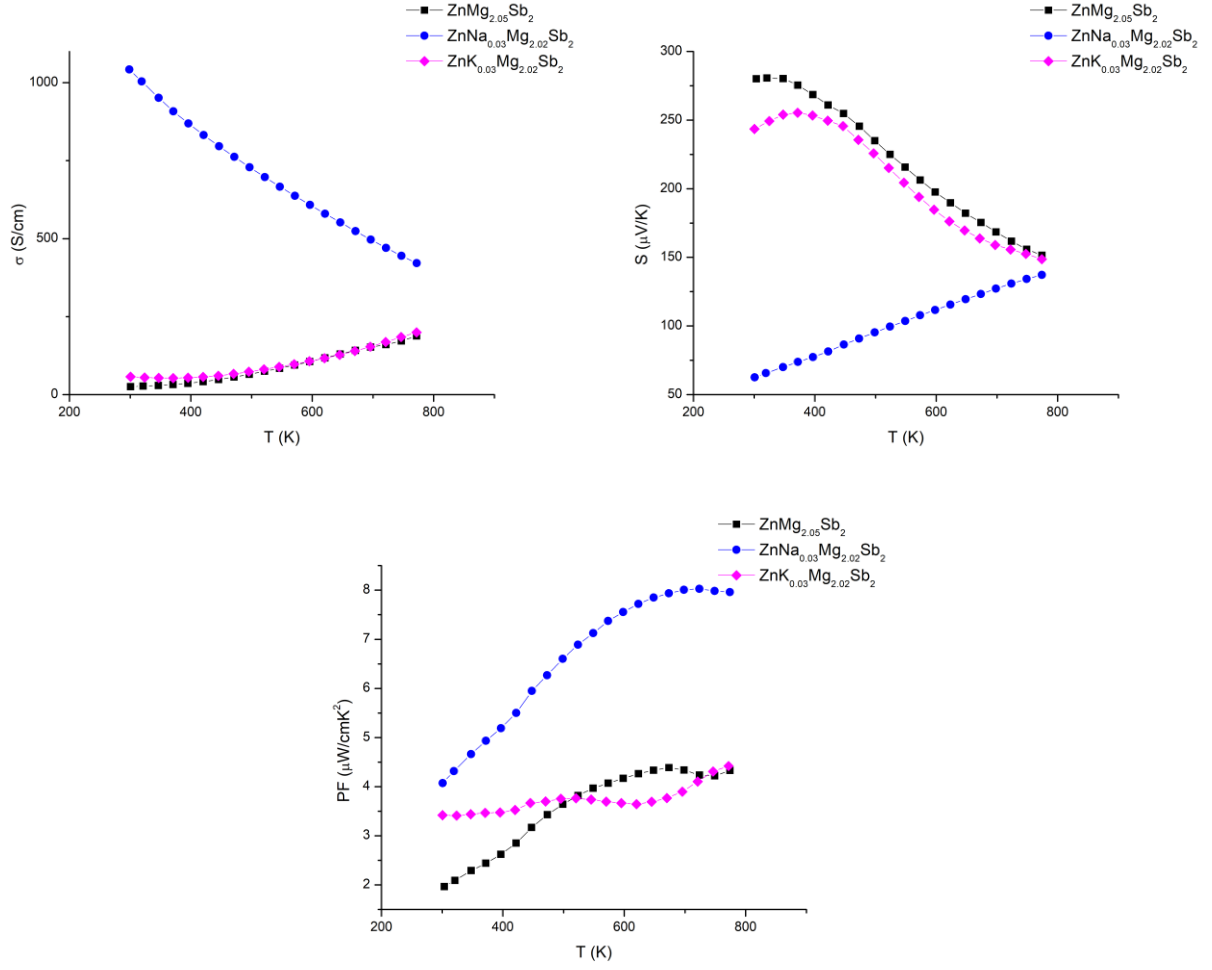


Figure 5.1. Temperature dependent charge transport properties of  $\text{ZnMg}_{2.05}\text{Sb}_2$  and  $\text{ZnK}_{0.03}\text{Mg}_{2.02}\text{Sb}_2$ .  $\text{ZnNa}_{0.03}\text{Mg}_{2.02}\text{Sb}_2$  is added for comparison purposes.

## 5.5 Conclusions

K doping into  $\text{ZnMg}_2\text{Sb}_2$  did not affect its thermoelectric properties. Property measurements show no significant differences between the  $\text{ZnMg}_{2.05}\text{Sb}_2$  and  $\text{ZnK}_{0.03}\text{Mg}_{2.02}\text{Sb}_2$  samples.

## Chapter 6. Failure of Zn/Bi co-doping in *p*-type Mg<sub>3</sub>Sb<sub>2</sub> based thermoelectric material

### 6.1 Abstract

While Zn substitution in Mg<sub>3</sub>Sb<sub>2</sub> yields a stable ZnMg<sub>2</sub>Sb<sub>2</sub> phase, the co-existence of both Bi and Zn in the Mg<sub>3</sub>Sb<sub>2</sub> structure cannot be achieved.

### 6.2 Introduction

By introducing heavier dopants into the Mg<sub>3</sub>Sb<sub>2</sub> structure, the lattice thermal conductivity  $\kappa_L$  would decrease due to increasing phonon scattering, triggered by mass differences. Bi doping in both *n*-type and *p*-type Mg<sub>3</sub>Sb<sub>2</sub> has been attempted by many groups, it was found to reduce thermal conductivity of the material. However, the thermal instability of the materials diminished. To decrease the lattice thermal conductivity, we attempted to introduce heavy Bi onto the Sb site in the Zn containing Mg<sub>3</sub>Sb<sub>2</sub> structure.

### 6.3 Experimental

Elemental Mg (powder, 99 wt.%, Sigma-Aldrich), Zn (powder, 99.995 wt.%, Sigma-Aldrich), Sb (chunks, 99.999 wt.%, 5N Plus), Bi (99.99 wt.%, Thermo Scientific) was weighed inside of an argon-filled glovebox according to the Zn<sub>0.5</sub>Mg<sub>2.5</sub>Sb<sub>2-x</sub>Bi<sub>x</sub> formula (*x* = 1, 2). The sample mixture was then ball milled and subjected to spark plasma sintering at 623 K for 30 minutes under 50 MPa. After discovering leaching of molten Bi, SPS temperature was reduced to 473 K. The ball milled powders and SPS pellets were analyzed with PXRD and EDS.



Please refer to *Chapter 3, Section 3.3 Experimental* for detailed experimental procedures.

The majority of the experimental procedures in this chapter followed the same protocol with the exception of starting materials and SPS temperature.

## 6.4 Results and discussions

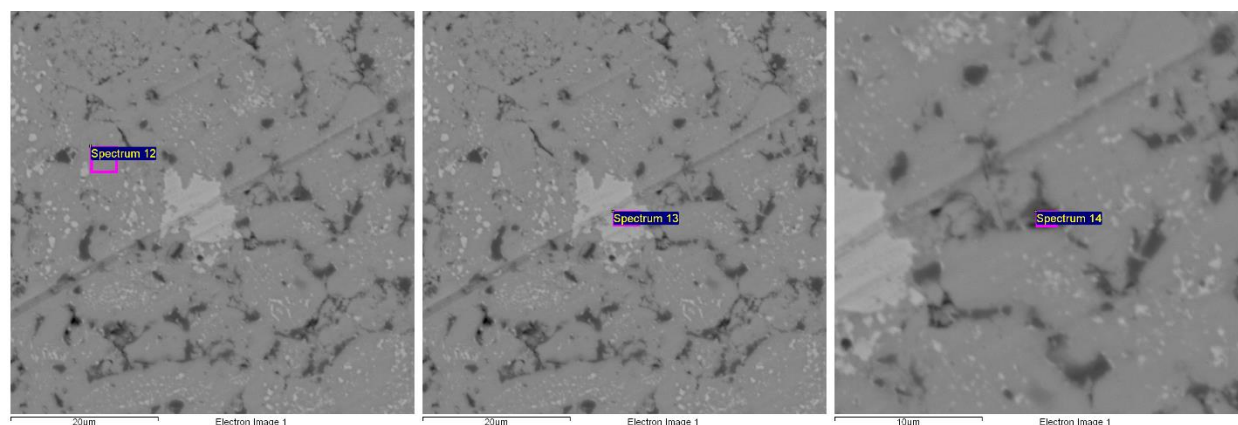
### 6.4.1 PXRD and SEM/EDS phase analysis

Table 6.1. PXRD phase analysis data of the ball milled Zn/Bi co-doped and Zn singly doped  $\text{Mg}_3\text{Bi}_2$  samples, as well as the sintered compositions.

| Composition   | Main phase (wt.%)                  | Bi (wt.%)                         | Sb (wt.%)       | Zn (wt.%)       |
|---|------------------------------------|-----------------------------------|-----------------|-----------------|
| BM –<br>$\text{Zn}_{0.5}\text{Mg}_{2.5}\text{BiSb}$       | $83.82 \pm 0.47$                   | $12.71 \pm 0.11$                  | $2.63 \pm 0.14$ | $0.83 \pm 0.10$ |
| SPS@623K –<br>$\text{Zn}_{0.5}\text{Mg}_{2.5}\text{BiSb}$ | <b><math>95.82 \pm 0.47</math></b> | <b><math>3.95 \pm 0.09</math></b> | $0.23 \pm 0.10$ | -               |
| BM –<br>$\text{Zn}_{0.5}\text{Mg}_{2.5}\text{Bi}_2$       | $56.41 \pm 0.38$                   | $38.70 \pm 0.45$                  | -               | $4.89 \pm 0.33$ |
| SPS@473K –<br>$\text{Zn}_{0.5}\text{Mg}_{2.5}\text{Bi}_2$ | $59.27 \pm 0.19$                   | $36.42 \pm 0.21$                  | -               | $4.31 \pm 0.15$ |

The SPS@623K –  $\text{Zn}_{0.5}\text{Mg}_{2.5}\text{BiSb}$  sample had a significant amount of leaked molten Bi during sintering. Therefore, the refined **Bi (wt.%)** amount for this sample is much lower than the actual value. To address Bi leaking during SPS, the subsequent samples containing both Zn and Bi were sintered at 473 K, below bismuth’s melting point of 544.6 K. However, as evident from the PXRD phase analysis, there were no significant changes between the ball milled and sintered samples. This suggests that Bi and Zn do not coexist in the  $\text{Mg}_3\text{Sb}_2$  structure.

Between the “BM –  $\text{Zn}_{0.5}\text{Mg}_{2.5}\text{BiSb}$ ” and “BM –  $\text{Zn}_{0.5}\text{Mg}_{2.5}\text{Bi}_2$ ” samples, the  $\text{Zn}_{0.5}\text{Mg}_{2.5}\text{BiSb}$  sample had significantly less Zn impurity. Again, this result suggests Zn and Bi are not compatible in the  $\text{Mg}_3\text{Sb}_2$  structure.



| Element | Atomic% | Element | Atomic% | Element | Atomic% |
|---------|---------|---------|---------|---------|---------|
| Mg      | 59.14   | -       |         | Mg      | 16.36   |
| Zn      | 1.79    | -       |         | Zn      | 73.28   |
| Bi      | 39.06   | Bi      | 100.00  | Bi      | 10.36   |

Table 6.2. SEM/EDS analysis of SPS  $\text{Zn}_{0.5}\text{Mg}_{2.5}\text{Bi}_2$ , sintered at 473 K under 50 MPa.

As evident from the EDS results in Table 6.2, the main phase in the SPS  $\text{Zn}_{0.5}\text{Mg}_{2.5}\text{Bi}_2$  sample consists of mainly Mg and Bi. The integrated 1.79 at. % of Zn is likely due to neighboring free Zn (dark spots) near the analyzed area (“Spectrum 12” in the left SEM image). The pure Bi and Zn rich inclusions (73.28 at. %) imply separation of the two elements. At high magnification ( $\sim 5,000$  magnification), the X-ray acquisition area is likely bigger than the selected area, hence contributions from the neighboring phases are sampled.

Since Cd belongs to the same group as Zn, the Cd/Bi co-doping was also attempted despite the slim chances for success. Based on the PXRD analysis, Cd and Bi do not coexist in the  $\text{Mg}_3\text{Sb}_2$  structure. Interestingly, amount of the main phase goes down after sintering at 523 K. Additionally, the decrease in Sb impurity and increase in elemental Bi suggests Sb replacement for Bi in the structure. Increase in the Cd amount suggests thermal decomposition.

Table 6.3. PXRD phase analysis of the ball milled and sintered Cd/Bi co-doped samples sintered at 523K.

| <b>Composition</b>                                     | <b>Main phase (wt.%)</b> | <b>Bi (wt.%)</b> | <b>Sb (wt.%)</b> | <b>Cd (wt.%)</b> |
|--|--------------------------|------------------|------------------|------------------|
| BM –<br>Cd <sub>0.5</sub> Mg <sub>2.5</sub> BiSb       | 83.43 ± 0.72             | 13.53 ± 0.16     | 1.36 ± 0.12      | 1.68 ± 0.06      |
| SPS@523K –<br>Cd <sub>0.5</sub> Mg <sub>2.5</sub> BiSb | 78.36 ± 2.66             | 18.38 ± 0.42     | -                | 3.26 ± 0.11      |

## 6.5 Conclusions

The leakage of molten Bi during sintering at 623 K indicates instability of the Zn/Bi co-doped Mg<sub>3</sub>Sb<sub>2</sub>. Zn doping of Mg<sub>3</sub>Bi<sub>2</sub> was unsuccessful and supports incompatibility of Zn and Bi in the Mg<sub>3</sub>Sb<sub>2</sub> structure. The SEM/ED analysis showed heterogenous phases, with Zn and Bi rich areas. The main phase mainly consists of Mg and Bi, suggesting Mg<sub>3</sub>Bi<sub>2</sub>. In summary, Zn and Bi cannot be co-doped into Mg<sub>3</sub>Sb<sub>2</sub> structure.

## Chapter 7. Failure of Pb doping of $\text{Mg}_3\text{Sb}_2$ based thermoelectric material

### 7.1 Abstract

While following the experimental procedures of Bhardwaj & Misra, 2014<sup>26</sup>, we could not prepare Pb doped  $\text{Mg}_3\text{Sb}_2$ . Molten Pb leaked out during the SPS and subsequent PXRD and SEM/EDS analysis showed no significant presence of Pb in the main phase.

### 7.2 Introduction

For a material to exhibit *p*-type behavior, the material generally should be electron deficient. The oxidation states and number of valence electrons are usually considered when deciding on the dopant. In  $\text{Mg}_3\text{Sb}_2$ , Mg exhibits a 2+ charge, and Sb exhibits a 3- charge. In the above sections, Na was a successful *p*-type dopant due to its ability to increase charge carrier mobility  $\mu$ . Li, Na, Ag and Cu are also *p*-type dopants due to their 1+ charge.

According to Bhardwaj & Misra,  $\text{Mg}_3\text{Sb}_{2-x}\text{Pb}_x$  ( $x = 0, 0.05, 0.1, 0.2, 0.3$ ) could be successfully synthesized. Pb, if substituted into the Sb site would act as a *p*-type dopant due to lower electron count and decrease lattice thermal conductivity  $\kappa_L$  due to increased mass difference.

### 7.3 Experimental

The experimental procedures in this section are based on the data by Bhardwaj & Misra, 2014<sup>26</sup>.

Elemental Mg (powder, 99 wt.%, Sigma-Aldrich), Sb (chunks, 99.999 wt.%, 5N Plus), Pb (99.9 wt.%, Thermo Scientific) were weighed inside of an argon-filled glovebox according to the  $\text{Mg}_{3.05}\text{Sb}_{1.8}\text{Pb}_{0.2}$  formula. The sample mixture was then ball milled and spark plasma sintered at 1073 K for 20 minutes under 50 MPa. PXRD and SEM/EDS analyses were performed on the consolidated pellet.

Please refer to *Chapter 3, Section 3.3 Experimental* for detailed experimental procedures. The majority of the experimental procedures in this chapter follow the same protocol with the exception of starting materials and SPS temperature.

## 7.4 Results and discussions

### 7.4.1 PXRD and SEM/EDS phase analysis

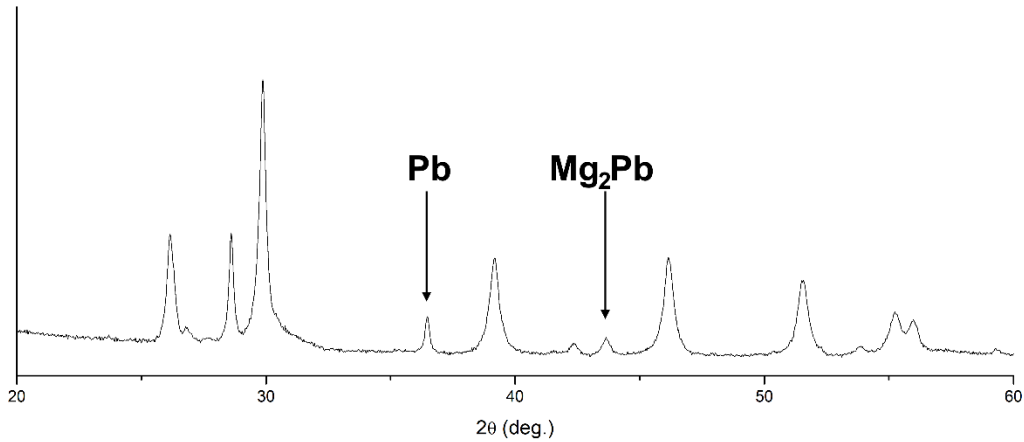


Figure 7.1. Powder X-ray diffraction pattern of 1073 K sintered  $\text{Mg}_{3.05}\text{Sb}_{1.8}\text{Pb}_{0.2}$ .

Table 7.1. Rietveld refined PXRD phase composition indicating Pb and  $\text{Mg}_2\text{Pb}$  impurity phases.

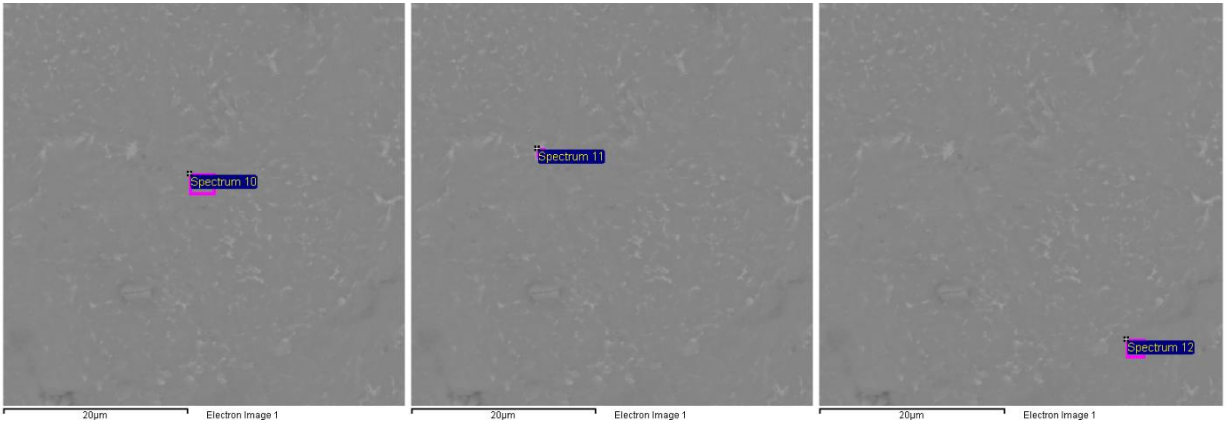
| Composition                                      | Main phase (wt.%) | Pb (wt.%)       | $\text{Mg}_2\text{Pb}$ (wt.%) |
|--|-------------------|-----------------|-------------------------------|
| $\text{Mg}_{3.05}\text{Sb}_{1.8}\text{Pb}_{0.2}$ | $92.82 \pm 3.78$  | $2.73 \pm 0.14$ | $4.45 \pm 0.22$               |

During SPS, molten Pb escaped from the graphite dies and therefore, the Rietveld refined PXRD phase composition in Table 7.1. understated the amount of the Pb impurity.

Interestingly, there was no Sb impurity but there Pb and Mg<sub>2</sub>Pb impurities. Assuming no Pb leakage, amount of the Pb impurity would be higher, but the Mg<sub>2</sub>Pb impurity would not change significantly, as the amount of Mg available is limited and dictated by the loading composition.

Table 7.2. PXRD lattice constants of the Mg<sub>3.05</sub>Sb<sub>1.8</sub>Pb<sub>0.2</sub> samples; Mg<sub>3</sub>Sb<sub>2</sub> is included from literature data <sup>13</sup> for comparison.

| Composition  | a = b     | c         | Cell Volume [Å <sup>3</sup> ] |
|--|-----------|-----------|-------------------------------|
| Mg <sub>3.05</sub> Sb <sub>1.8</sub> Pb <sub>0.2</sub> | 4.5611(7) | 7.231(1)  | 130.28(3)                     |
| Mg <sub>3</sub> Sb <sub>2</sub> <sup>13</sup>          | 4.568(3)  | 7.229(4)  | 130.6(4)                      |
| Mg <sub>3</sub> Sb <sub>2</sub><br>(Experimental)      | 4.5634(4) | 7.2337(7) | 130.46(2)                     |



| Element | Atomic% | Element | Atomic% | Element | Atomic% |
|---------|---------|---------|---------|---------|---------|
| Mg      | 59.83   | Mg      | 60.87   | Mg      | 54.83   |
| Sb      | 38.09   | Sb      | 23.83   | Sb      | 28.25   |
| Pb      | 2.08    | Pb      | 15.29   | Pb      | 2.67    |
| -       | -       | -       | -       | Cr      | 2.46    |
| -       | -       | -       | -       | Fe      | 11.79   |

Table 7.3. SEM/EDS analysis of the SPS Mg<sub>3.05</sub>Sb<sub>1.8</sub>Pb<sub>0.2</sub> sample.

One could argue that the EDS analysis of the main phase indicates presence of Pb although in lower amounts (2.08% as opposed to the target ~4%Pb). However, there is inaccuracy in the signal acquisition at the high magnification (~5,000 magnification), as neighboring phases, which have heavy Pb segregation, can interfere with the EDS integration. Assuming Pb is successfully doped in the structure, there should be no significant Pb segregations and no Mg<sub>2</sub>Pb (as according to PXRD). However, presence of elemental Pb and Pb leakage during SPS suggest little to no Pb incorporation into the Mg<sub>3</sub>Sb<sub>2</sub> structure.

We have also attempted the Zn/Pb co-doping. The ZnMg<sub>2.05</sub>Sb<sub>1.9</sub>Pb<sub>0.1</sub> sample was sintered at temperature 573 K, below the Pb melting point of 600 K to prevent Pb leakage.

Table 7.4. Rietveld refined PXRD phase composition.

| <b>Composition</b>                                       | <b>Main phase (wt.%)</b> | <b>Pb (wt.%)</b> | <b>Mg<sub>2</sub>Pb (wt.%)</b> |
|--|--------------------------|------------------|--------------------------------|
| Mg <sub>3.05</sub> Sb <sub>1.8</sub> Pb <sub>0.2</sub>   | 92.82 ± 3.78             | 2.73 ± 0.14      | 4.45 ± 0.22                    |
| ZnMg <sub>2.05</sub> Sb <sub>1.9</sub> Pb <sub>0.1</sub> | 94.49 ± 0.77             | 5.51 ± 0.13      | -                              |

Although there was no Pb leakage, the large amount of Pb impurities suggests no Pb incorporation. Interestingly, there was no formation of Mg<sub>2</sub>Pb at the sintering temperature of 573 K as opposed to the previous sintering temperature of 1073 K sintered. Absence of Mg<sub>2</sub>Pb can be explained using the Mg – Pb binary phase diagram:

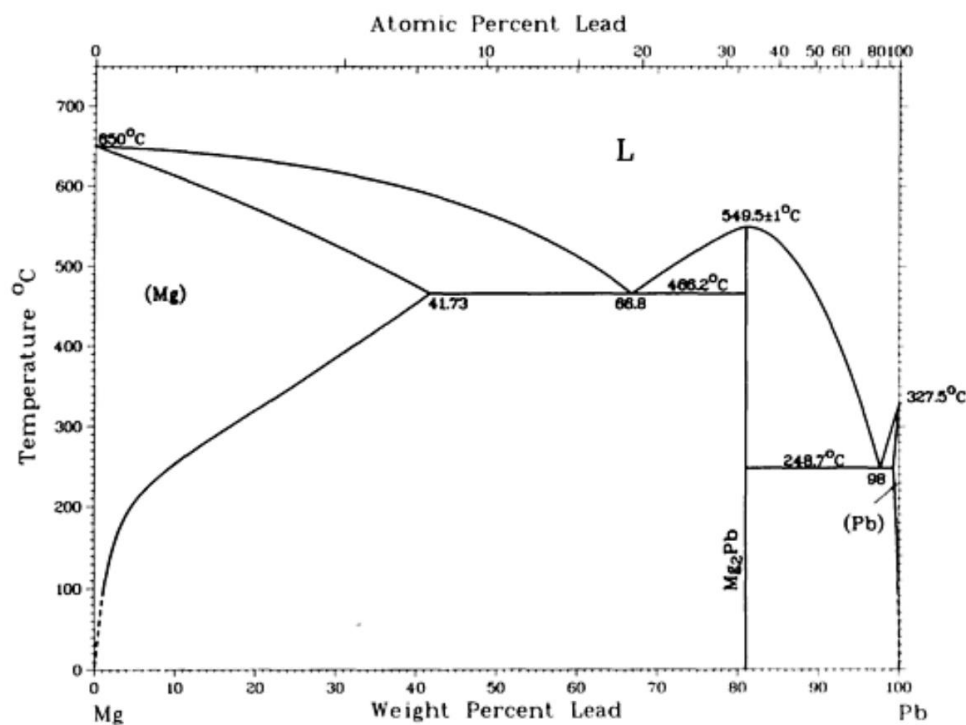


Figure 7.2 Binary phase diagram of magnesium-lead.

The sintering temperature at 573 K (300 °C) did not produce any liquid phases, and any reactions in the solid state are too slow to yield Mg<sub>2</sub>Pb. On the other hand, the sintering temperature of 1073 K (800 °C) would melt Pb, Mg, or their mixture, and subsequent cooling would produce Mg<sub>2</sub>Pb.

## 7.5 Conclusions

This study has failed to reproduce the data from Bhardwaj & Misra, 2014<sup>26</sup>. There was no mentioning of Mg<sub>2</sub>Pb impurity nor the leakage of Pb in their study. Based on our data, we believe little to no Pb is into the Mg<sub>3</sub>Sb<sub>2</sub> structure.



## Chapter 8. Na/Bi co-doping in *p*-type Mg<sub>3</sub>Sb<sub>2</sub> based thermoelectric material

### 8.1 Abstract

Synthesis of Na<sub>x</sub>Mg<sub>3.05-x</sub>SbBi ( $x = 0.015, 0.03$ ) was achieved during ball milling. However, Bi impurity developed in both samples after spark plasma sintering at 623 K suggesting material instability. Charge transport properties were measured. While Na doping increased electrical conductivity, the Seebeck coefficient was significantly lower than for the Zn/Na co-doped samples (Chapter 3), resulting in a poor power factor.

### 8.2 Introduction

With the introduction of heavy Bi in the Mg<sub>3</sub>Sb<sub>2</sub> structure, an increase in mass-difference phonon scattering and low thermal conductivity are expected. Due to the lower electronegativity of Bi<sup>3-</sup> in comparison to Sb<sup>3-</sup>, a reduction in band gap and an increase in electrical conductivity  $\sigma$  are also anticipated.

### 8.3 Experimental

Elemental Mg (powder, 99 wt.%, Sigma-Aldrich), Sb (chunks, 99.999 wt.%, 5N Plus), Bi (99.99 wt.%, Thermo Scientific) as well as the precursor NaSb, obtained in Chapter 3, were weighed inside of an argon-filled glovebox s according to the composition Na<sub>x</sub>Mg<sub>3.05-x</sub>SbBi ( $x = 0.015, 0.03$ ). The mixtures were then ball milled and subjected to spark plasma sintering at 623

K for 30 minutes under the pressure of 50 MPa. The ball milled powders and consolidated samples were analyzed with PXRD and EDS. Charge transport properties were also measured.

Please refer to *Chapter 3, Section 3.3 Experimental* for detailed experimental procedures.

The majority of the experimental procedures in this thesis follow the same protocol except for starting materials and SPS temperature.

## 8.4 Results and discussions

### 8.4.1 PXRD and SEM/EDS phase analysis

With the substitution of  $\text{Sb}^{3-}$  with larger  $\text{Bi}^{3-}$  anion, the lattice parameters of the Bi doped  $\text{Mg}_3\text{Sb}_2$  structure increased significantly (Table 8.2)

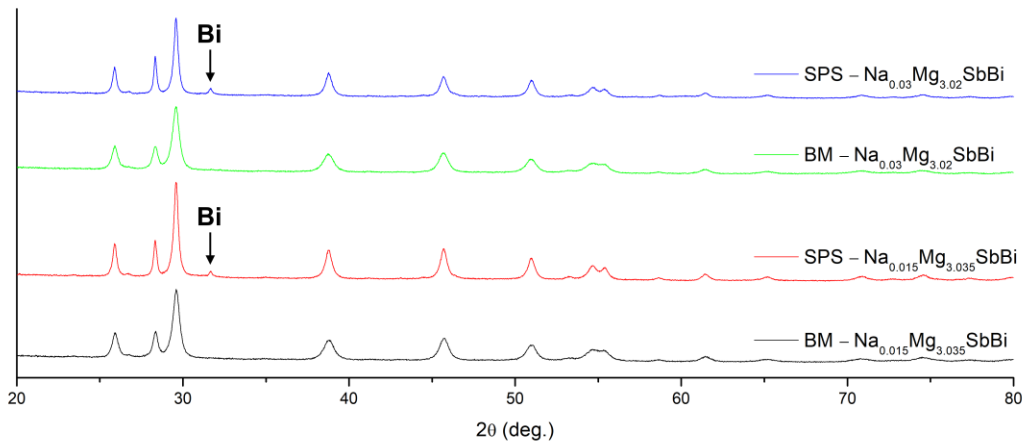


Figure 8.1. Powder X-ray diffraction patterns of ball milled (BM) and sintered (SPS)  $\text{Na}_x\text{Mg}_{3.05-x}\text{SbBi}$  ( $x = 0.015, 0.03$ ), showing Bi impurity.

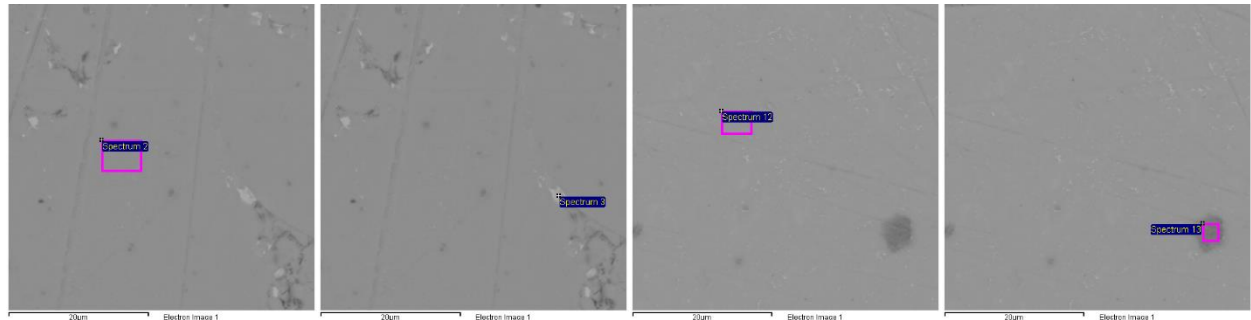
Both samples decomposed during SPS at 623 K, as evident from significant amount of elemental Bi in the PXRD patterns. Brighter areas in the SEM images (Table 8.3), corresponding to elemental Bi, also support material instability during the SPS.

Table 8.1. PXRD phase analysis of the ball-milled (BM) and SPS  $\text{Na}_x\text{Mg}_{3.05-x}\text{SbBi}$  samples ( $x = 0.015, 0.03$ ).

| Composition   | Main phase (wt.%) | Bi (wt.%)       |
|---|-------------------|-----------------|
| BM – $\text{Na}_{0.015}\text{Mg}_{3.035}\text{SbBi}$  | $99.90 \pm 2.20$  | $0.10 \pm 0.08$ |
| SPS – $\text{Na}_{0.015}\text{Mg}_{3.035}\text{SbBi}$ | $97.65 \pm 2.09$  | $2.35 \pm 0.08$ |
| BM – $\text{Na}_{0.03}\text{Mg}_{3.02}\text{SbBi}$    | $99.80 \pm 2.23$  | $0.20 \pm 0.08$ |
| SPS – $\text{Na}_{0.03}\text{Mg}_{3.02}\text{SbBi}$   | $97.14 \pm 2.97$  | $2.86 \pm 0.12$ |

Table 8.2. Rietveld refined lattice parameters of the ball-milled (BM) and SPS  $\text{Na}_x\text{Mg}_{3.05-x}\text{SbBi}$  samples ( $x = 0.015, 0.03$ ). The lattice parameters of  $\text{Mg}_3\text{Sb}_2$  are included for comparison.

| Composition   | a = b     | c         | Cell volume [ $\text{\AA}^3$ ] |
|---|-----------|-----------|--------------------------------|
| BM – $\text{Na}_{0.015}\text{Mg}_{3.035}\text{SbBi}$  | 4.6088(4) | 7.3113(7) | 134.49(2)                      |
| SPS – $\text{Na}_{0.015}\text{Mg}_{3.035}\text{SbBi}$ | 4.6081(3) | 7.3079(4) | 134.39(1)                      |
| BM – $\text{Na}_{0.03}\text{Mg}_{3.02}\text{SbBi}$    | 4.6114(4) | 7.3119(7) | 134.65(2)                      |
| SPS – $\text{Na}_{0.03}\text{Mg}_{3.02}\text{SbBi}$   | 4.6081(4) | 7.3051(6) | 134.34(2)                      |
| $\text{Mg}_3\text{Sb}_2$                              | 4.5634(4) | 7.2337(7) | 130.46(2)                      |



| Element | Atomic% | Element | Atomic% | Element | Atomic% | Element | Atomic% |
|---------|---------|---------|---------|---------|---------|---------|---------|
| Mg      | 58.86   | Mg      | 10.93   | Mg      | 58.99   | Mg      | 18.13   |
| Sb      | 21.15   | Sb      | 2.23    | Sb      | 20.94   | Sb      | 2.70    |
| Bi      | 19.99   | Bi      | 86.84   | Bi      | 18.77   | Bi      | 4.36    |
| -       | -       | -       | -       | Na      | 0.31    | Na      | 0.05    |
| -       | -       | -       | -       | -       | -       | Cr      | 12.13   |
| -       | -       | -       | -       | -       | -       | Fe      | 54.53   |

|   |   |   |   |   |   |    |      |
|---|---|---|---|---|---|----|------|
| - | - | - | - | - | - | Ni | 1.94 |
| - | - | - | - | - | - | Si | 6.17 |

Table 8.3. SEM/EDS s analysis of  $\text{Na}_{0.015}\text{Mg}_{2.035}\text{SbBi}$  (left figure: main phase; second from the left: Bi segregation), and  $\text{Na}_{0.03}\text{Mg}_{2.02}\text{SbBi}$  (second from the right: main phase; right: steel contamination). The absence of Na in  $\text{Na}_{0.015}\text{Mg}_{2.035}\text{SbBi}$  could be due to the low limit of detection (LOD) of the TESCAN VEGA SEM.

## 8.4.2 Charge transport properties

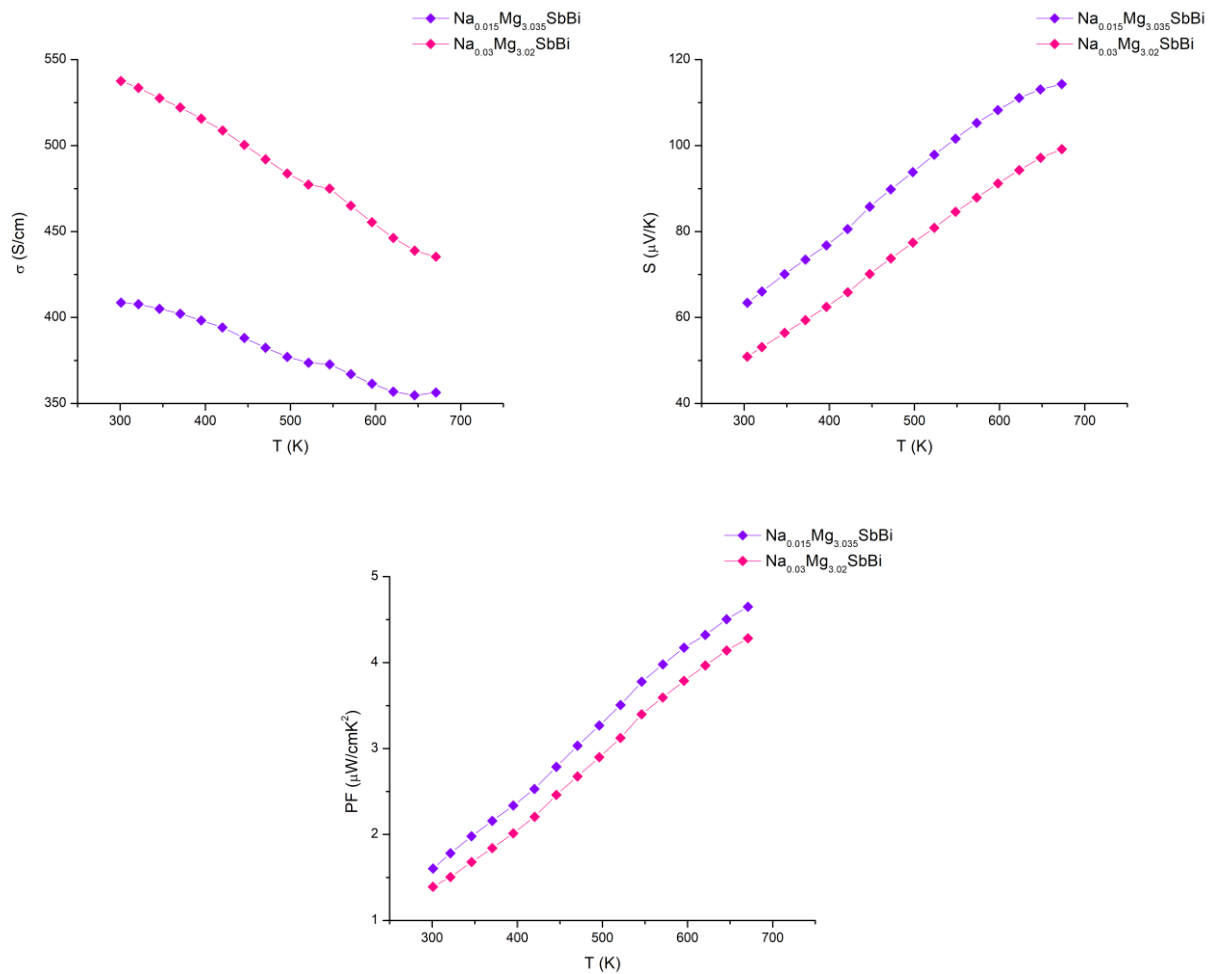


Figure 8.2. Charge transport properties of  $\text{Na}_{0.015}\text{Mg}_{3.035}\text{SbBi}$  and  $\text{Na}_{0.03}\text{Mg}_{3.02}\text{SbBi}$

The composition with more Na has a higher electrical conductivity,  $\sigma$ , which is expected and follows the trends observed in the previous chapters. However, both compositions suffer

from the low Seebeck coefficient,  $S$ ; for comparison, the thermopower of  $\text{ZnNa}_{0.015}\text{Mg}_{2.035}\text{Sb}_2$  ranges from  $\sim 86 \mu\text{V/K}$  to  $\sim 157 \mu\text{V/K}$ . Consequently, the samples exhibit low power factors; for comparison, the PF of  $\text{ZnNa}_{0.015}\text{Mg}_{2.035}\text{Sb}_2$  is between  $\sim 4.7 \text{ W/mK}$  and  $7.9 \text{ W/mK}$ .

However, the main goal of doping Bi is to enhance the material thermal transport properties by lowering the lattice thermal conductivity  $\kappa_L$ . Unfortunately, the thermal transport studies on the two samples were not performed as the samples decomposed at the 623 K temperature (Figure 8.1, Table 8.1). Appearance of molten Bi with high vapor pressure during thermal diffusivity measurements would damage the expensive NETZSCH LFA 457 Microflash instrument. To increase material stability, one lowers the Bi amount.

## 8.5 Conclusions

The  $\text{Na}_{0.015}\text{Mg}_{3.035}\text{SbBi}$  and  $\text{Na}_{0.03}\text{Mg}_{3.02}\text{SbBi}$  sample show reasonable electrical conductivity which increases with the Na amount. However, both compositions suffer from low thermopower and therefore exhibit very low PF. Both samples are thermally unstable, and more stable phases need to be synthesized for thermal conductivity measurements.

## Chapter 9. Thesis conclusion

Na is found to be an effective *p*-type charge carrier dopant as it significantly increases electrical conductivity in various Na-doped compositions. Ag doping also increases electrical conductivity, however, improvements in electrical properties are inferior to the Na doped samples. Moreover, Ag doping likely narrows the band gap of materials, which leads to a bipolar effect at mid-temperatures. Although Na doping improves electrical properties, the Na-doped samples have poorer thermal properties due to an increased electronic part in the total thermal conductivity.

Cd was successfully doped into the  $\text{Mg}_3\text{Sb}_2$  material. However, all Cd-doped samples have poor thermal stability as they decompose during spark plasma sintering or electrical property measurement at high temperatures.

While Li and Na are reported as effective *p*-type dopants, doping with K does not improve the electrical properties.

While  $\text{Mg}_3\text{Sb}_2$  could be successfully doped with either Zn or Bi, co-doping with both Zn and Bi at high dopant amounts failed. It appears that Zn and Bi cannot co-exist together in the  $\text{Mg}_3\text{Sb}_2$  structure.

## Chapter 10. Future works

The main achievement of this work is the Zn and Na co-doped compositions, showing increased power factor and  $zT$  values. However, the doped compositions display a higher total thermal conductivity due to a larger electronic contribution. To counter this issue, a heavier dopant Bi can be employed. While Zn and Bi substitutions were unsuccessful, lower doping levels of Zn and Bi should be considered as they may provide sufficient reduction in the thermal conductivity without affecting the electrical properties significantly. Hence, Na doping coupled with heavier Zn and Bi, should be explored with the goal of achieving the desired thermoelectric properties.

## References

1. Ahmadpour, F., Kolodiazhnyi, T., & Mozharivskyj, Y. (2007). Structural and physical properties of  $\text{Mg}_{3-x}\text{Zn}_x\text{Sb}_2$  ( $x=0-1.34$ ). *Journal of Solid State Chemistry*, 180(9), 2420–2428. <https://doi.org/10.1016/j.jssc.2007.06.011>
2. Chen, C., Li, X., Li, S., Wang, X., Zhang, Z., Sui, J., Cao, F., Liu, X., & Zhang, Q. (2018). Enhanced thermoelectric performance of P-type  $\text{Mg}_3\text{Sb}_2$  by lithium doping and its tunability in an anionic framework. *Journal of Materials Science*, 53(23), 16001–16009. <https://doi.org/10.1007/s10853-018-2555-2>
3. Wang, H., Chen, J., Lu, T., Zhu, K., Li, S., Liu, J., & Zhao, H. (2018). Enhanced thermoelectric performance in P-type  $\text{Mg}_3\text{Sb}_2$  via lithium doping. *Chinese Physics B*, 27(4), 047212. <https://doi.org/10.1088/1674-1056/27/4/047212>
4. Shuai, J., Wang, Y., Kim, H. S., Liu, Z., Sun, J., Chen, S., Sui, J., & Ren, Z. (2015). Thermoelectric properties of Na-doped Zintl compound:  $\text{Mg}_3\text{-Na Sb}_2$ . *Acta Materialia*, 93, 187–193. <https://doi.org/10.1016/j.actamat.2015.04.023>
5. Ren, Z., Shuai, J., Mao, J., Zhu, Q., Song, S., Ni, Y., & Chen, S. (2018). Significantly enhanced thermoelectric properties of P-type  $\text{Mg}_3\text{Sb}_2$  via co-doping of Na and Zn. *Acta Materialia*, 143, 265–271. <https://doi.org/10.1016/j.actamat.2017.10.015>
6. Song, L., Zhang, J., & Iversen, B. B. (2017). Simultaneous improvement of power factor and thermal conductivity via Ag doping in P-type  $\text{Mg}_3\text{Sb}_2$  thermoelectric materials. *Journal of Materials Chemistry A*, 5(10), 4932–4939. <https://doi.org/10.1039/c6ta08316a>



7. Kannan, V. P., Lourdhusamy, V., Paulraj, I., Madanagurusamy, S., & Liu, C.-J. (2024). Significantly enhanced thermoelectric performance of p-type  $\text{Mg}_3\text{Sb}_2$  via Zn substitution on Mg(2) site: Optimization of hole concentration through Ag Doping. *ACS Applied Materials & Interfaces*, 16(43), 58677–58688.  
<https://doi.org/10.1021/acsami.4c12868>
8. Cromer, D. T. (1959). The crystal structure of NaSB. *Acta Crystallographica*, 12(1), 41–45. <https://doi.org/10.1107/s0365110x59000123>
9. Agne, M. T., Imasato, K., Anand, S., Lee, K., Bux, S. K., Zevalkink, A., Rettie, A. J. E., Chung, D. Y., Kanatzidis, M. G., & Snyder, G. J. (2018). Heat capacity of  $\text{Mg}_3\text{Sb}_2$ ,  $\text{Mg}_3\text{Bi}_2$ , and their alloys at high temperature. *Materials Today Physics*, 6, 83–88.  
<https://doi.org/10.1016/j.mtphys.2018.10.001>
10. Vapor pressures of the chemical elements. Vapor pressures of the Chemical Elements, vapor pressure of metals and halogens from -150 degrees C to 3500 degrees C including lead, aluminum, zinc, iodine, copper, indium, iodine, magnesium, selenium, lithium, iron, sodium and gallium. (n.d.). <https://www.powerstream.com/vapor-pressure.htm>
11. Kauzlarich, S. M., Brown, S. R., & Jeffrey Snyder, G. (2007). Zintl phases for thermoelectric devices. *Dalton Transactions*, (21), 2099.  
<https://doi.org/10.1039/b702266b>
12. Li, J., Liu, K., Ma, X., Yang, Z., Yi, L., Mao, J., & Zhang, Q. (2024). Improvement of the thermoelectric properties of P-type  $\text{Mg}_3\text{Sb}_2$  by Mg-site double substitution. *Inorganic Chemistry*, 63(43), 20126–20132. <https://doi.org/10.1021/acs.inorgchem.4c00522>

13. Martinez-Ripoll, M., Haase, A., & Brauer, G. (1974). The crystal structure of  $\alpha$ -mg<sub>3</sub>sb<sub>2</sub>. Acta Crystallographica Section B Structural Crystallography and Crystal Chemistry, 30(8), 2006–2009. <https://doi.org/10.1107/s0567740874006285>
14. Tang, X., Zhang, B., Zhang, X., Wang, S., Lu, X., Han, G., Wang, G., & Zhou, X. (2020). Enhancing the thermoelectric performance of P-type mg<sub>3</sub>sb<sub>2</sub> via codoping of Li and CD. ACS Applied Materials & Interfaces, 12(7), 8359–8365. <https://doi.org/10.1021/acsami.9b23059>
15. Xiao, S., Peng, K., Zhou, Z., Wang, H., Zheng, S., Lu, X., Han, G., Wang, G., & Zhou, X. (2023). Realizing CD and ag codoping in P-type mg<sub>3</sub>sb<sub>2</sub> toward high thermoelectric performance. Journal of Magnesium and Alloys, 11(7), 2486–2494. <https://doi.org/10.1016/j.jma.2021.09.012>
16. Tiadi, M., Battabyal, M., Jain, P. K., Chauhan, A., Satapathy, D. K., & Gopalan, R. (2021). Enhancing the thermoelectric efficiency in P-type MG<sub>3</sub>sb<sub>2</sub> via mg site co-doping. Sustainable Energy & Fuels, 5(16), 4104–4114. <https://doi.org/10.1039/d1se00656h>
17. Zachariasen, W. H. (1926). Die kristallstruktur der telluride von zink, cadmium und quecksilber. Nor. Geol. Tidsskr, 8, 302-306.
18. Xu, Y. N., & Ching, W. Y. (1993). Electronic, optical, and structural properties of some wurtzite crystals. Physical Review B, 48(7), 4335.
19. Müller, W. J., & Löffler, G. (1933). Zur Kenntnis der Färbung von gefälltem Cadmiumsulfid. Angewandte Chemie, 46(33), 538-539.

20. Sakiyama, H., Abiko, T., Ito, M., Mitsuhashi, R., Mikuriya, M., & Waki, K. (2016). Conformational analysis of an octahedral zinc(ii) complex with six dimethylsulfoxide. *Polyhedron*, 119, 512–516. <https://doi.org/10.1016/j.poly.2016.09.039>
21. Mixer/Mill 8000M\*. HORIBA. (n.d.). <https://www.horiba.com/int/scientific/products/detail/action/show/Product/mixer-mill-8000m-981/>
22. Ratzker, B., & Sokol, M. (2023). Exploring the capabilities of high-pressure spark plasma sintering (HPSPS): A review of Materials Processing and properties. *Materials & Design*, 233, 112238. <https://doi.org/10.1016/j.matdes.2023.112238>
23. Guignard, J., Prakasam, M., & Largeteau, A. (2022). High pressure (HP) in Spark Plasma Sintering (SPS) processes: Application to the polycrystalline diamond. *Materials*, 15(14), 4804. <https://doi.org/10.3390/ma15144804>
24. Liu, L., Li, X., He, Q., Xu, L., Cao, X., Peng, X., Meng, C., Wang, W., Zhu, W., & Wang, Y. (2017). Sintering dense boron carbide without grain growth under high pressure. *Journal of the American Ceramic Society*, 101(3), 1289–1297. <https://doi.org/10.1111/jace.15282>
25. Deller, K., & Eisenmann, B. (1977). Ternäre Erdalkali-element(v)-Verbindungen AMG2B2 MIT A = ca, sr, ba und b = as, Sb, Bi / ternary alkaline earth-element(v)-compounds AMG2B2 with a = ca, sr, ba and b = as, Sb, Bi. *Zeitschrift Für Naturforschung B*, 32(6), 612–616. <https://doi.org/10.1515/znb-1977-0602>

26. Bhardwaj, A., & Misra, D. K. (2014). Enhancing thermoelectric properties of a P-type  $\text{mg}_3\text{sb}_2$ - based Zintl phase compound by PB substitution in the anionic framework. RSC Adv., 4(65), 34552–34560. <https://doi.org/10.1039/c4ra04889j>
27. [J.C. Slater](#) (1964). "Atomic Radii in Crystals". The Journal of Chemical Physics. **41** (10): 3199–3204. [Bibcode:1964JChPh..41.3199S](#). [doi:10.1063/1.1725697](#).

## Supplementary Information



Figure S1.1. Photograph of the NaSb polycrystalline precursor inside of an Ar glovebox. Needle-shaped crystals are visible on the surface.



Figure S1.2a. Photograph of the KSb polycrystalline precursor extracted from the carbon-coated quartz tube inside the Ar-filled glovebox.



Figure S1.2b. Photograph of the KSb crystal inside the Ar-filled glovebox.

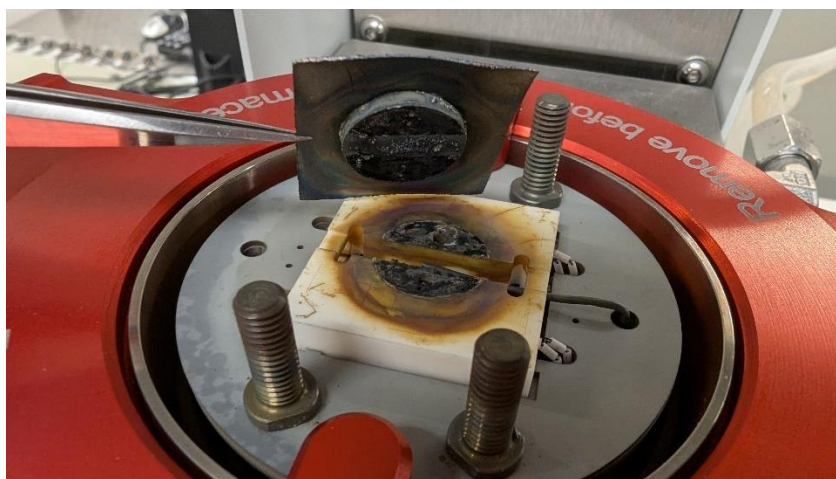


Figure S1.3a. Cadmium-damaged silica/alumina sample stage of the NETZSCH SBA 458 Nemesis instrument. Brown deposits strongly suggest the presence of cadmium oxide. The Cd-containing sample pellet was stuck to the graphite paper (as shown at the top).

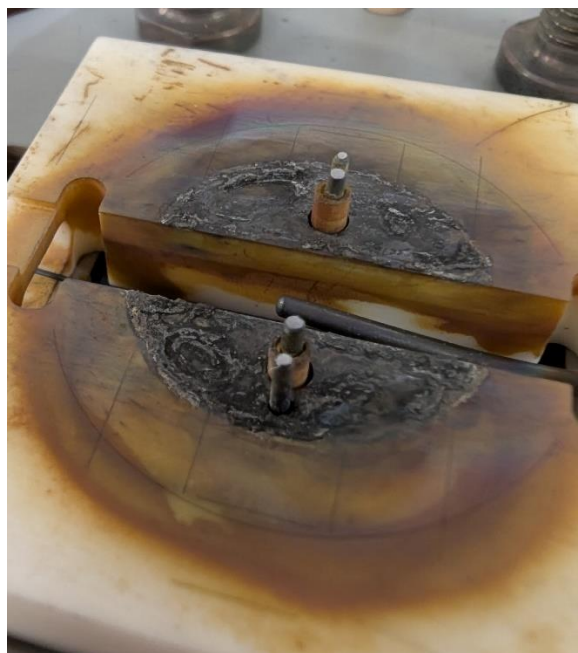


Figure S1.3b. A close-up photograph of the cadmium-damaged silica/alumina sample stage of the NETZSCH SBA 458 Nemesis instrument.





Figure S1.4a. Photograph of a cadmium-covered walls inside the SPS chamber. The clean chamber is shiny. The dull grey deposit is elemental cadmium.



Figure S1.4b. Photograph of the cadmium leakage from the SPS graphite die/punch.